

1 **Genomic evidence supports a clonal diaspora model for metastases of esophageal**  
2 **adenocarcinoma**

3  
4 Ayesha Noorani<sup>1</sup>, Xiaodun Li<sup>1</sup>, Martin Goddard<sup>2</sup>, Jason Crawte<sup>1</sup>, Ludmil B. Alexandrov<sup>3</sup>, Maria  
5 Secrier<sup>4</sup>, Matthew D. Eldridge<sup>4</sup>, Lawrence Bower<sup>4</sup>, Jamie Weaver<sup>1</sup>, Pierre Lao-Sirieix<sup>1</sup>, Inigo  
6 Martincorena<sup>5</sup>, Irene Debiram-Beecham<sup>1</sup>, Nicola Grehan<sup>1</sup>, Shona MacRae<sup>1</sup>, Shalini  
7 Malhotra<sup>6</sup>, Ahmad Miremadi<sup>6</sup>, Tabitha Thomas<sup>7</sup>, Sarah Galbraith<sup>8</sup>, Lorraine Petersen<sup>7</sup>,  
8 Stephen D. Preston<sup>2</sup>, David Gilligan<sup>9</sup>, Andrew Hindmarsh<sup>10</sup>, Richard H. Hardwick<sup>1</sup>, Michael R.  
9 Stratton<sup>5</sup>, David C. Wedge<sup>11, 12\*</sup> and Rebecca C. Fitzgerald<sup>1\*</sup>

10 <sup>1</sup>MRC Cancer Unit, University of Cambridge, Biomedical Campus, Cambridge, CB2 0XZ, UK

11 <sup>2</sup>Department of Histopathology, Papworth Hospital NHS Trust, Cambridge, CB23 3RE, UK

12 <sup>3</sup>Theoretical Biology and Biophysics (T-6), Los Alamos National Laboratory, New Mexico, 87545, USA

13 <sup>4</sup>Cancer Research UK Cambridge Research Institute, Cambridge, CB2 0RE, UK

14 <sup>5</sup>Wellcome Trust Sanger Institute, Cambridge, CB10 1SA, UK

15 <sup>6</sup>Department of Histopathology, Cambridge University Hospitals NHS Foundation Trust, Cambridge, CB2 0QQ,  
16 UK

17 <sup>7</sup>Arthur Rank Hospice Charity, Cambridge, CB22 3FB, UK

18 <sup>8</sup>Department of Palliative Care, Cambridge University Hospitals NHS Foundation Trust, Cambridge, CB2 0QQ,  
19 UK

20 <sup>9</sup>Oncology Centre, Cambridge University Hospitals NHS Foundation Trust, Cambridge, CB2 0QQ, UK

21 <sup>10</sup>Oesophago-Gastric Centre, Cambridge University Hospitals NHS Foundation Trust, Cambridge, CB2 0QQ, UK

22 <sup>11</sup>Big Data Institute, University of Oxford, Oxford, OX3 7LF, UK

23 <sup>12</sup>Oxford NIHR Biomedical Research Centre, Oxford, OX4 2PG, UK

24

25

26 \*Correspondence to Rebecca Fitzgerald rcf29@mrc-cu.cam.ac.uk or David Wedge david.wedge@bdi.ox.ac.uk

27 **Abstract (95 words)**

28 The poor outcomes in esophageal adenocarcinoma (EAC) prompted us to interrogate the  
29 pattern and timing of metastatic spread. Whole genome sequencing and phylogenetic  
30 analysis of 388 samples across 18 EAC cases demonstrated in 90% of cases that multiple  
31 subclones from the primary tumor spread very rapidly from the primary site to form  
32 multiple metastases, including lymph nodes and distant tissues, a mode of dissemination  
33 that we term 'clonal diaspora'. Metastatic subclones at autopsy were present in tissue and  
34 blood samples from earlier time-points. These findings have implications for our  
35 understanding and clinical evaluation of EAC.

36

37 **Introduction**

38 Metastatic spread to distant sites accounts for the majority of cancer deaths<sup>1</sup>.  
39 Understanding the anatomical extent of disease is essential to determine the optimum  
40 treatment strategy. This is challenging since cancer continually evolves at a microscopic  
41 scale, often beyond the resolution of clinical imaging techniques. Furthermore, the patterns  
42 of metastatic spread are often unpredictable in terms of time-course and anatomical  
43 location. Treatments may therefore be unnecessarily toxic (e.g. radical lymphadenectomy  
44 and chemotherapy) or insufficiently aggressive, leading to high recurrence rates<sup>2-4</sup>.

45 Esophageal cancer is the sixth most common cause of cancer-related death worldwide and  
46 the current median survival time is still <1 year<sup>5</sup>. Incidence rates for esophageal  
47 adenocarcinoma (EAC) have risen sharply and it is now the predominant subtype in  
48 developed countries. Prognosis is highly variable for EAC patients as shown by the wide  
49 range of 5-year survival (18-47% with lymph node involvement), making it difficult to advise  
50 patients when embarking on a long course of grueling treatment<sup>2,6</sup>.

51 Theoretical and experimental studies attempt to understand how tumor cell populations  
52 respond to selective pressures over time<sup>7</sup>. A number of models of tumor evolution have  
53 been proposed, including linear, branching, neutral and punctuated evolution, but the  
54 extent to which these are specific to a given cancer type or co-occur is controversial<sup>8,9</sup>.

55 Genome sequencing studies have attempted to delineate different models of evolution<sup>10</sup>.

56 However, many of these studies have focused solely on evolution within the primary site,  
57 and knowledge of how genetic diversity emerges during metastasis remains limited. The

58 lack of understanding is in part due to the practical challenge of collecting multiple samples  
59 over space and time from advanced stage cancer patients.

60 To better understand the evolution of EAC, we designed a prospective study with extensive  
61 sampling over time including samples from diagnosis, surgery and at warm autopsy (Figure  
62 1). We used whole genome sequencing (WGS) at high depth (50x), to identify mutations,  
63 and at shallow (1x) coverage, to track known variants, to interrogate the clonal architecture  
64 across time and space.

65

## 66 **Results**

### 67 **Genomic architecture of 18 cases**

68 Eighteen cases were included in the study and the clinical demographics of these cases are  
69 shown in Supplementary Table 1 and 2, with details of the individual samples given in  
70 Supplementary Table 3 and 4. In the first part of the study (Figure 1a, Extended Data Fig.  
71 1,2) we used 50x WGS to construct a phylogenetic tree for each case, to understand the  
72 relationship between the primary and metastatic tumors (Figure 2, Extended Data Fig. 3 ,  
73 Supplementary Figure 1, Supplementary Table 3, 4). Mutation clustering was performed,  
74 and the fractions of tumor cells carrying each set of mutations (Cancer Cell Fraction, CCF)  
75 within each sample were used to determine: 1) the clonal and sub-clonal architecture of  
76 each tumor (subclonal CCF <95%, clonal CCF  $\geq$  95%); 2) the hierarchy of events; and 3) the  
77 distance of these sub-clonal or clonal clusters from the most recent common ancestor  
78 (MRCA) (Figure 1a, Extended Data Fig. 1,2). The CCF and number of single nucleotide  
79 variants (SNVs) associated with each clone and subclone are shown in Supplementary Table  
80 5 and 6, as is the tumor purity of each sample using the Battenberg algorithm<sup>11</sup>, in  
81 Supplementary Table 7 and the confidence intervals of the clonal and subclonal CCFs in  
82 Supplementary Table 8. Detailed information on experimental design is provided in the Life  
83 Sciences Reporting Summary.

84 These analyses enabled us to construct phylogenetic trees (Methods). In all cases we  
85 observed a long trunk compared to the rest of the tree (median 19,034 SNVs, IQR 11,299-  
86 63,908), consistent with previous studies in EAC<sup>12,13</sup>. The median size of clonal or subclonal  
87 clusters across all cases was 3,069 SNVs (IQR 1332-63908) and only 2/157 contained fewer  
88 than 200 SNVs (S1\_3 and P5\_11), Extended Data Fig. 3 and Supplementary Table 6.

89 The key driver events<sup>14,15</sup> are depicted on each phylogenetic tree (Figure 2 and Extended  
90 Data Fig. 3). The events identified as most frequent in previous studies occurred in the  
91 trunks of the phylogenetic trees, consistent with their previous classification as drivers. *TP53*  
92 was mutated in the trunk of 16 out of 18 cases, consistent with our knowledge of the  
93 disease<sup>14,16-19</sup>. Amplifications (gene names in red) were often truncal, but also observed on  
94 the branches of the phylogenetic tree, providing evidence of divergence during later  
95 evolutionary stages (Figure 2, Extended Data Fig. 3). The majority of events in driver genes  
96 were copy number alterations (CNAs) rather than SNVs or InDels (Figure 2, Extended Data  
97 Fig. 3)<sup>14,19,20</sup>. There was no significant difference in the overall number of structural variants  
98 between primary and metastatic samples (p=0.41, generalized linear model; Extended Data  
99 Fig. 4b). However, a larger proportion of structural variants in metastatic samples were  
100 retro-transpositions of mobile elements than in the primary samples (p=0.045, Extended  
101 Data Fig. 4c). This contrasts with pancreatic cancer, where deletions and fold-back  
102 inversions are more common in metastases, and breast cancer where tandem duplications  
103 dominate<sup>21</sup>. Interestingly, the high rate of L1 transposon activity in EAC has recently been  
104 associated with high activity in the germline<sup>22</sup>. Our results suggest a further increase in L1  
105 activity in metastatic EAC. Furthermore, the proportion of structural variants found uniquely  
106 in metastases or in primary sites was higher than that of SNVs (Figure 2, Extended Data 4a),  
107 suggesting an increase in genomic instability in later stages of the disease. However, it  
108 cannot be ruled out that some structural variants have not been identified in every sample  
109 as a result of lower sensitivity in the detection of structural variants than SNVs.

110 Across the eighteen cases, 8 mutational signatures were observed, consistent with previous  
111 studies<sup>23-26</sup> (Figure 3a), with varying prevalence across the cases. None of the signatures that  
112 we observe in patients in our cohort who had oncologic therapy have been associated with  
113 treatment with alkylating antineoplastic agents<sup>27</sup>, platinum therapy<sup>28</sup> or radiation therapy<sup>29</sup>.

114

### 115 **Early seeding of oligometastases**

116 Ten of eighteen patients (S3, S4, P1-4, P6, P8-10) had both nodal and solid organ  
117 metastases, allowing a direct comparison of the genomic architecture between different  
118 metastatic sites (Figure 2).

119 In four of these ten cases, an isolated clone or subclone confined to 1 or 2 distant  
120 metastases, i.e. an oligometastasis, depicted as a dashed black node on the first branch of

121 the phylogenetic tree, shared the highest congruence to the MRCA, (P1, P4, P10, S3 in  
122 Figure 2; Subclones P1\_2, P4\_3, P10\_2, S3\_2 in Supplementary Table 5). In P1, this clone  
123 (P1\_2) was observed only in the primary tumor and a pleural metastasis. In S3 and P4, the  
124 clone involved in this isolated seeding was identified at a single distant site and not in the  
125 primary tumor (S3\_2: liver metastasis (D1), P4\_3: para-aortic lymph node (L3)). In P10, the  
126 early seeding clone (P10\_2) was shared between a distant para-aortic node and a sub-clonal  
127 metastasis in the right hemi-diaphragm. The subclones associated with these isolated  
128 seeding events showed little divergence from the MRCA across these 4 cases (median 1,913  
129 SNVs, range 832-8,591), suggesting early seeding to distant metastases. Notably, in P9 a  
130 subclone (P9\_10, Supplementary Table 5) was found in a premalignant area of Barrett's  
131 esophagus and a pleural metastasis but not in any of four areas of the primary tumor  
132 subject to 50x WGS. This subclone lineage shares no variants with the main lineage and  
133 appears to be an independent second cancer (Figure 2).

#### 134 **A single clone gives rise to multiple metastatic sites**

135 A striking observation was that 9/10 cases had a clone (outlined in red on the phylogenetic  
136 tree in Figure 2) that was followed by dispersion of multiple subclones from the primary to  
137 discrete metastatic sites, resulting in a model of metastasis that we term 'clonal diaspora'.  
138 In most cases, this dispersion was visually stellate in nature, this being defined as a feature  
139 of a phylogenetic tree involving 3 or more branches leading from a single founder clone (see  
140 details in Discussion). The subclones forming diasporas were located in both primary and  
141 metastatic tissue in eight cases (P1, P2, P3, S4, P4, P6, P8, P10) and in P9 were unique to  
142 metastases (Figure 2). The only two cases lacking a stellate pattern on the phylogenetic tree  
143 were P10 and S3. The latter is a non-autopsy case with limited tissue sampling and the early  
144 distant seeding in this case is consistent with a pattern of parallel evolution (Figure 2).

145

#### 146 **Subclonal spread is not constrained by location or tissue**

147 In the second step of the study we tracked the spread of metastases across a wider range of  
148 lymph node and distant tissue sites by performing 1x WGS in a further 248 tissue samples  
149 from 6 autopsy cases (Figure 1a,c). We did not call new mutations, as this would not be  
150 possible at 1x sequencing, but used this method to detect the spread of clones and  
151 subclones previously identified using 50x WGS (bioinformatic validation of methods in

152 Extended Data Fig. 5 and 6, Supplementary Note; wet lab validation in Extended Data Fig. 7,  
153 Supplementary Table 9). The samples used in this part of the study are outlined in  
154 Supplementary Table 10. The median size of subclonal and clonal clusters (identified  
155 previously at 50x WGS) that we aimed to detect using 1x WGS was 3,784 (IQR 1,966-49,955).  
156 Sample sites were grouped according to their similarity based on the presence of subclones  
157 and clones previously detected with 50x WGS (Supplementary Note). The resulting groups  
158 of samples are color coded and numbered, and each sample site, colored by group, is shown  
159 on the adjacent body map (Figure 4, see also Supplementary Note). Notably, the samples  
160 that grouped together based on shared clonal origins were widely dispersed anatomically.  
161 Four out of six cases with extensive spatial sampling (Figure 4) had liver metastases  
162 evaluated and three of these contained samples that were more similar to local lymph node  
163 metastases than neighboring liver metastases (P4, P6, P8 but not P10). The high number of  
164 groups within the liver (up to four) suggested seeding by multiple subclones (seen in P4, P6,  
165 P8), whereas the single group in the liver of P10 (orange, group 3) indicated seeding by a  
166 common progenitor or a set of closely related cells.  
167 A comparison of lymph node location and genomic contiguity showed no evidence of  
168 tropism, i.e. genomically similar lymph nodes did not occupy nearby anatomical locations.  
169 Lymph nodes above and below the diaphragm were frequently seeded from common  
170 events (P2: groups 1, 3; P4: groups 5, 6; P6: group 5; P8: groups 2, 3,5, 6; P10: group 4), at  
171 odds with a progression from local to distant nodes. Similarly, a comparison of lymph node  
172 and solid organ metastases showed scant evidence for tropism, with the exception of P1  
173 (Supplementary Note). This patient underwent surgical resection and subsequently had  
174 metastatic disease recurrence. In this cancer, separate subclones seeded lymph node and  
175 pleural metastases (Figure 2, 4). Notably, the distant metastasis (D1) was an early branching  
176 oligometastasis whereas the lymph nodes (L1, L2) constituted the later diaspora event  
177 (black and red circles, respectively, in Figure 2).  
178 We further traced regions of the primary tumor at autopsy that had similar subclonal  
179 compositions to each of the metastases, shown as adjacent tumor maps (Figure 4, bottom  
180 left of each case). Subclones occupied spatially distinct areas in the primary tumor.  
181 We also looked for driver amplifications post MRCA or post diaspora on a per case basis and  
182 identified selection in 6/10 cases. However, this is likely to be an under-estimate, since there  
183 may be non-copy number drivers present in additional cases. The ratio of non-synonymous

184 to synonymous SNVs (dN/dS) was analyzed across all cases in order to assess the presence  
185 or absence of positive selection<sup>30</sup>. Results indicated positive selection in both clonal and  
186 subclonal genomes, albeit with lower levels of selection within subclones (Extended Data  
187 Fig. 8).

188

### 189 **Metastatic spread is rapid in EAC**

190 To examine the timing and speed of metastatic spread we analyzed base substitution  
191 mutational signatures, particularly the aging signature which features a predominance of  
192 C>T transition in the NpCpG trinucleotide context (Figure 1a, Figure 3).

193 Signature 1 arises from the spontaneous or enzymatic deamination of methylated cytosines,  
194 which is an endogenous process that occurs continuously in both healthy and cancerous  
195 cells. This has been shown to act as a molecular clock<sup>27,31-35</sup>, and was therefore used here as  
196 a method to examine the temporal relationship between metastases. Using a previously  
197 described method for deconvolving mutational signatures<sup>35</sup>, we observed that signature 1  
198 was present in the trunk but absent in all subclones that constituted diaspora (following the  
199 red parental clone in Figure 2) for P2, P4, P6, P9, P10, S4 and it was significantly reduced for  
200 P1 (21% to 3%) and P3 (16% to 9%) (Wilcoxon signed rank test  $p=0.039$ , Figure 3c). To  
201 account for the possibility that the number of signature 1 mutations in branch subclones  
202 was below the resolution of our deconvolution methods, we also identified the number of  
203 mutations with the characteristic feature of signature 1, i.e. C>T mutations in a CpG context.  
204 To estimate the time of appearance of diaspora, we compared the number of these  
205 characteristic mutations that occurred along the trunk to the parental red clone marking the  
206 onset of diaspora with those that occurred on the longest branch leading from this point.  
207 The median proportion of such mutations occurring prior to the onset of diaspora was 0.911  
208 (Figure 3b). Thus, in the majority of cases one might deduce that little time has elapsed  
209 between the appearance of the cell that is ancestral to disseminating cells and the individual  
210 cells that seeded each of the metastases. With the exception of P8, the proportion of  
211 mutations attributed to signature 1 was significantly lower after the parental (red) clone on  
212 the phylogenetic tree ( $p < 9.1 \times 10^{-5}$ , Chi-squared test across all cases; Figure 3c) suggesting  
213 an increase in the activity of other processes in later evolutionary stages (Supplementary  
214 Table 11). Of note, there was an increase in the proportion of signature 3 in subclonal SNVs

215 compared to clonal SNVs (Wilcoxon signed rank test  $p=0.019$ , Figure 3b), suggesting failure  
216 of DNA double strand break repair is predominantly a late-stage event in EAC.

217

### 218 **Early detection from diagnostic samples**

219 Next, we investigated eight cases (P1-4, P6, P8-10) for which the esophageal diagnostic FFPE  
220 biopsy or surgical sample (primary tumor at resection for P1 and lymph node from surgery  
221 for P9) were available, with a median time prior to autopsy of 12 months (range 5-30  
222 months) (Figure 1). The diagnostic sample for P1 was snap frozen and sequenced to 50x  
223 (Figure 2; highlighted with \* in Extended Data Fig. 9), while 1x WGS was performed on the  
224 remainder of the cases. Between 8% and 36% of the subclones and clones observed in  
225 samples taken from autopsy were also present in the diagnostic samples (Supplementary  
226 Note and Extended Data Fig. 9). In six cases, all subclones identified from the biopsy samples  
227 were also found in the primary samples from autopsy. Two diagnostic endoscopic samples  
228 from P4 also contained many of the mutations found in the lymph node L2 at autopsy,  
229 which had not been previously identified in the primary tumor at autopsy (Figure 2,  
230 subclone P4\_17, Supplementary Table 5). Similarly, the biopsy sample from P10 contained a  
231 substantial number of mutations from both the oligometastasis that seeded D2 and L4  
232 (Supplementary Table 5, P10\_2), and the lineage that later metastasized to multiple sites  
233 (Figure 2). Notably, P4 and P10 had shorter survival times after diagnosis than the remaining  
234 patients (5 and 4 months, respectively).

235

### 236 **Plasma sample analysis at autopsy and earlier time-points**

237 We assessed the clonal composition of circulating tumor DNA (ctDNA) at earlier time-points  
238 in seven blood samples from five cases (Figure 1, Figure 5a,c; Extended Data Fig. 10,  
239 Supplementary Table 12). Combined 1x WGS subclone/clone detection, copy number  
240 aberrations and *TP53* fraction using digital PCR data are displayed for two of these cases (P6  
241 and P10) in Figure 5a. Notably, P6 was a patient being treated with curative intent and had  
242 no radiological evidence of distant nodal or organ metastases at the time of clinical staging.  
243 However, at the time of diagnosis mutations from the truncal cluster and three subclonal  
244 clusters later found in the metastases were already present in the plasma (Figure 5a) along  
245 with amplifications in *MYC* and *GATA4*. Case S4 is noteworthy as the brain metastases (D1,  
246 D2 in Figure 2) appeared to have originated from a subclone shared between the primary



247 and a local lymph node, both of which were removed at the time of surgery (Extended Data  
248 Fig. 10c). However, mutations from the truncal cluster and four subclonal clusters were  
249 already present in ctDNA prior to radiological recurrence.

250 In eight cases, plasma was available from rapid autopsy. One case (P3) failed wet lab SNV  
251 validation and was hence removed from the SNV subclone analysis (Supplementary Note).  
252 Analysis of ctDNA demonstrated that in all cases the truncal cluster from autopsy was also  
253 represented in plasma (Figure 5c). In addition, mutations from between 0 and 7 subclonal  
254 clusters were identified from plasma (Figure 5c). The ratio of mutations detected from each  
255 subclone was very consistent between blood from earlier time points and autopsy (Pearson  
256  $r$  range [0.851, 0.994], maximum P-value  $8.9 \times 10^{-4}$ ) and in 2 of 5 cases the proportion of  
257 mutations detected was higher in the earlier sample, suggesting an opportunity for earlier  
258 detection of heterogeneous cancer cell populations. Further, subclonal proportions  
259 estimated from exome sequencing of plasma samples were highly correlated with those  
260 from 1x WGS (Supplementary Table 9).

261 The majority of driver CNAs identified in the MRCA of each tumor from 50x WGS of tissue  
262 samples were also identified in plasma both at autopsy and at earlier time-points (Figure  
263 5a,b). In addition, MET amplification, which was not present in the MRCA in P1 (Figure 2),  
264 was identified in plasma both at autopsy and an earlier time point (Extended Data Fig. 10a),  
265 suggesting opportunities for early detection of metastatic subclones. Notably, however,  
266 amplifications found only in oligometastases or in post-diaspora subclones from 50x  
267 sequencing were not identified in plasma, despite many of them being detected in 1x  
268 sequencing of tissue samples (Figure 5b). A plausible explanation for this observation is that  
269 each of the many metastasizing subclones contributed insufficient material to the sum of  
270 detected ctDNA to enable confident detection of CNAs.

271

## 272 **Discussion**

273 We have gathered multiple lines of evidence which suggest that, for the majority of EACs, a  
274 complex mode of spread is operative. These lines of evidence can be summarized as follows  
275 (Figure 6). We observe multiple subclones, each seeding multiple metastatic sites. These  
276 subclones are frequently derived from a single parental clone, generally resulting in a  
277 stellate pattern on the phylogenetic tree. Metastases in solid organs can bypass nodal  
278 involvement and samples within solid organ sites frequently resemble distant metastases

279 more closely than neighboring metastases within the same organ, i.e. no tropism is  
280 observed. All metastases appear to have spread directly from the primary site, with little or  
281 no evidence of metastasis-to-metastasis seeding.

282 These features differ in some important respects from previously described models of  
283 metastasis and we propose that they may constitute a distinct, additional model of  
284 evolution. We suggest that this pattern be referred to as a 'diaspora', by extension of the  
285 anthropological term to cancer<sup>36</sup>. Within this context, it is associated with the observation  
286 that multiple cell populations in metastatic sites are directly linked to the primary site of  
287 origin and that individual subclones seed multiple tissue types, analogous to a diaspora  
288 crossing multiple national boundaries.

289 A number of features were frequently associated with this phenomenon (Figure 6), with  
290 nine of the cases (all except S3) displaying at least two of the four following features: i)  
291 stellate pattern on the phylogenetic tree defined as three or more subclones emerging from  
292 the founder clones; ii) lack of signature 1 mutations post MRCA or post-diaspora; iii) spread  
293 of subclones to multiple organs of different type; iv) evidence for selection in post diaspora  
294 genotypes.

295 Until recently the genomic architectures of metastatic samples have not been defined with  
296 enough resolution to discern temporal or spatial patterns of metastatic spread. Several  
297 distinct patterns are now emerging which are not necessarily mutually exclusive or cancer-  
298 type specific. In pancreatic cancer, Yachida et al. demonstrated that distant organ seeding  
299 was a late event consistent with a linear progression model<sup>24</sup>. In prostate cancer, linear  
300 progression is often succeeded by multiple waves of seeding<sup>37</sup>. The same study further  
301 demonstrated widespread subclonal evolution in metastases and metastasis-to-metastasis  
302 spread, in keeping with the relatively long longevity of prostate cancer. Strikingly, a stellate  
303 pattern was not observed in any of the cases in that study, despite using a similar design to  
304 that used here.

305 In Supplementary Table 13 we compare the features of our proposed Diaspora model to the  
306 previously posited linear<sup>38</sup> and parallel<sup>8</sup> models. Whereas the linear model predicts that a  
307 single subclone seeding lymph node sites is followed by transmission to distant organs, the  
308 diaspora model posits simultaneous seeding of multiple sites directly from the primary.  
309 Unlike the parallel model, the diaspora model implies that metastasis formation occurs after  
310 the majority of evolution has occurred in the primary tumor, resulting in multiple subclones

311 found in common between primary and metastatic tumors. Lymphatic and distant  
312 metastases in colon cancer have been shown to arise from independent subclones in the  
313 primary tumor with disparate evolutionary trajectories<sup>39</sup>. In contrast, in EAC we find that  
314 individual subclones frequently seed both lymph node and distant organs suggesting that  
315 disparate trajectories for nodal and solid organ metastases do not exist for this disease  
316 (Figure 2, 3). Of note we acknowledge that, despite the extensive and systematic sampling  
317 across all autopsy cases, further sampling may add further branches to our phylogenetic  
318 tree, although this is unlikely to affect the diaspora event itself.

319 In common with the Big Bang Model proposed for colorectal cancer<sup>40</sup>, our model predicts  
320 the occurrence of highly branching phylogenies. However, the Big Bang Model proposes  
321 neutral dynamics, whereas we observe strong evidence for selection in subclonal  
322 populations in the form of dN/dS ratios and the occurrence of subclonal driver  
323 amplifications (Figure 2, Extended Data Figure 8, Supplementary Figure 2). Moreover, the  
324 clonal maps of the primary tumor demonstrate subclones that occupy spatially discrete  
325 areas of the primary tumor (Figure 4), in contrast to the intermixed subclones predicted by  
326 the Big Bang Model<sup>40</sup>.

327 The sequence of events in metastatic progression may have clinical implications that require  
328 further study (Supplementary Table 13). Clonal architecture in EAC defies anatomical  
329 location of lymph node stations and distant sites, which is the current basis for the TNM  
330 staging and determines whether curative therapy is appropriate. It has been suggested that  
331 the high recurrence rate, 52% within one year, results from seeding of distant metastases  
332 that are not detected at the time of diagnosis<sup>26</sup>. This study provides molecular evidence for  
333 this observation and highlights the need for different systemic approaches to disease  
334 management, including consideration of more aggressive adjuvant therapy which is not  
335 currently the mainstay of treatment<sup>41-44</sup>. With advances in the sensitivity of ctDNA assays,  
336 metastatic subclones may be detectable in the blood, helping to determine when systemic  
337 therapy is required post-surgery and in detecting heterogeneity of acquired resistance<sup>45</sup>.  
338 Copy number variation in plasma may also be a future early detection strategy<sup>46</sup>.

339

340 The occurrence of metastasis is a pivotal event in the life history of a cancer. Understanding  
341 the drivers behind such an event would have potential relevance to patient stratification  
342 and predicting and preventing metastatic spread<sup>47</sup>. While we have identified many drivers

343 on the trunks of the trees, prior to diaspora (Figure 2), we cannot be certain which event, if  
344 any, was the immediate trigger of diaspora in individual cases. In a number of cases,  
345 diaspora was coincident with an increase in the proportion of signature 3 mutations,  
346 associated with failure of DNA double-strand break-repair by homologous recombination  
347 (Figure 3b). Our findings are in keeping with the failure of DNA repair driving the  
348 appearance of genomic heterogeneity. Whether the heterogeneity observed is itself the  
349 driver of diaspora or merely a symptom is an important area for future study. Our  
350 investigations of the potential drivers of diaspora were limited to genomic factors, and  
351 further multi-platform studies looking at epigenetic and transcriptomic factors are other  
352 important avenues of future research. We anticipate that analyses of single cells or small  
353 clusters from primary sites, disseminated tumor cells and circulating tumor cells will also  
354 yield finer resolution of the processes of dissemination and metastasis.  
355 In cancer there are currently very few in-depth studies examining the spatial and temporal  
356 evolution of metastases<sup>48</sup>. Further studies are required to ascertain the extent to which our  
357 diaspora theory pertains to other cancers.

358

## 359 **Acknowledgements**

360 Above all, we are indebted to the patients who donated tissue samples to this project and  
361 thank them and their families who supported them through it. We would also like to thank  
362 the following individuals for their help with study set-up, patient liaison and tissue  
363 collection, Ben Smith, Nyrai Chinyama, Vijay Sujendran, Peter Safranek, Athanosios Xanthos,  
364 Tara Nuckcheddy-Grant, Rachel de la Rue, Sebastian Zeki, Rachael Fels Elliott, Peter Collins,  
365 Kitty Puttock, Sophie Rabey and staff at Arthur Rank Hospice and Luke A Wylie for scientific  
366 discussion and contribution. We would like to thank the Oesophageal Cancer Clinical and  
367 Molecular Stratification (OCCAMS) Consortium for providing the vehicle through which  
368 funding for the International Cancer Genome Consortium (ICGC) was obtained. We are  
369 grateful to Professor Simon Tavaré, FRS for his guidance and support for the esophageal  
370 whole genome sequencing project as a part of the International Cancer Genome Consortium  
371 (ICGC). We would like to thank Jo Westmoreland, LMB visual aids for her graphic art  
372 expertise. Thanks also go to the Cancer Research UK Cambridge Institute Genomics Core for  
373 their technical expertise. We thank the Human Research Tissue Bank, which is supported by  
374 the National Institute for Health Research (NIHR) Cambridge Biomedical Research Centre,

375 from Addenbrooke's Hospital. Additional infrastructure support was provided from the  
376 CRUK funded Experimental Cancer Medicine Centre in Cambridge. Computation by DCW  
377 used the Oxford Biomedical Research Computing (BMRC) facility, a joint development  
378 between the Wellcome Centre for Human Genetics and the Big Data Institute supported by  
379 Health Data Research UK and the NIHR Oxford Biomedical Research Centre.  
380 Ayesha Noorani was funded through an MRC Clinical Research Fellowship. The work was  
381 funded through the above and an MRC core grant (RG84369) and an NIHR Research  
382 Professorship (RG67258) to Rebecca Fitzgerald. Funding for sample sequencing (50x WGS)  
383 was through the International Cancer Genome Consortium and was funded by a programme  
384 grant from Cancer Research UK (RG66287). All OCCAMS samples which were part of the  
385 surgical/endoscopy cohort were obtained from Cambridge patients. David Wedge is funded  
386 by the Li Ka Shing foundation and the National Institute for Health Research (NIHR) Oxford  
387 Biomedical Research Centre.

388

### 389 **Author Contributions**

390 AN designed and implemented the rapid autopsy study, collected the samples, performed  
391 the experiments, analyzed data and wrote the manuscript. MG and S.D.P contributed  
392 expertise in pathology and sample collection for the rapid autopsy study. ID-B and NG  
393 assisted in study implementation, and along with JC, assisted with sample collection at  
394 autopsy. M.S performed the structural variant analysis. M.D.E performed genomic data  
395 generation and QC. LB conducted data management. XL, PL-S and JW were involved with  
396 autopsy sample collection, advice on experiments and data analysis, and XL contributed to  
397 experiments, paper writing, and figure design. LA and IM assisted with data analysis. NG  
398 assisted with study Implementation. SMac coordinated the sequencing of samples from the  
399 OCCAMS project and contributed to paper writing. SM and AM provided pathology  
400 data. TT, SG, LP and DG assisted in implementation and ethical conduct of the autopsy  
401 study. R.H.H and AH were involved in surgical sample collection and providing surgical  
402 expertise. M.R.S contributed to critical evaluation of the study data and manuscript. D.C.W  
403 was responsible for data analysis, paper writing, and assuring integrity of data. The OCCAMS  
404 consortium was the vehicle through which the infrastructure and funding was obtained to  
405 support the study and the consortium contributed to discussions on the ICGC data and the

406 clinical ramifications. R.C.F provided grant funding and was responsible for study design,  
407 supervision of the project, writing the paper and assuring integrity of the data.

408

409 The authors declare no competing interests.

410 **References**

411

- 412 1. Sporn, M.B. The war on cancer. *Lancet* **347**, 1377-81 (1996).
- 413 2. Waterman, T.A. *et al.* The prognostic importance of immunohistochemically detected  
414 node metastases in resected esophageal adenocarcinoma. *Ann Thorac Surg* **78**, 1161-  
415 9; discussion 1161-9 (2004).
- 416 3. Matsuda, S., Takeuchi, H., Kawakubo, H. & Kitagawa, Y. Three-field lymph node  
417 dissection in esophageal cancer surgery. *J Thorac Dis* **9**, S731-S740 (2017).
- 418 4. Lou, F. *et al.* Esophageal cancer recurrence patterns and implications for surveillance.  
419 *J Thorac Oncol* **8**, 1558-62 (2013).
- 420 5. Smyth, E.C. *et al.* Oesophageal cancer. *Nat Rev Dis Primers* **3**, 17048 (2017).
- 421 6. Cunningham, D. *et al.* Capecitabine and oxaliplatin for advanced esophagogastric  
422 cancer. *N Engl J Med* **358**, 36-46 (2008).
- 423 7. Greaves, M. & Maley, C.C. Clonal evolution in cancer. *Nature* **481**, 306-13 (2012).
- 424 8. Klein, C.A. Parallel progression of primary tumours and metastases. *Nat Rev Cancer*  
425 **9**, 302-12 (2009).
- 426 9. Davis, A., Gao, R. & Navin, N. Tumor evolution: Linear, branching, neutral or  
427 punctuated? *Biochim Biophys Acta* **1867**, 151-161 (2017).
- 428 10. Yates, L.R. & Campbell, P.J. Evolution of the cancer genome. *Nat Rev Genet* **13**, 795-  
429 806 (2012).
- 430 11. Nik-Zainal, S. *et al.* The life history of 21 breast cancers. *Cell* **149**, 994-1007 (2012).
- 431 12. Murugaesu, N. *et al.* Tracking the genomic evolution of esophageal adenocarcinoma  
432 through neoadjuvant chemotherapy. *Cancer Discov* **5**, 821-831 (2015).
- 433 13. Gerstung, M. *et al.* The evolutionary history of 2,658 cancers. *bioRxiv* (2017).
- 434 14. Secrier, M. *et al.* Mutational signatures in esophageal adenocarcinoma define  
435 etiologically distinct subgroups with therapeutic relevance. *Nat Genet* **48**, 1131-41  
436 (2016).
- 437 15. Dulak, A.M. *et al.* Gastrointestinal adenocarcinomas of the esophagus, stomach, and  
438 colon exhibit distinct patterns of genome instability and oncogenesis. *Cancer Res* **72**,  
439 4383-93 (2012).
- 440 16. Weaver, J.M. *et al.* Ordering of mutations in preinvasive disease stages of esophageal  
441 carcinogenesis. *Nat Genet* **46**, 837-43 (2014).
- 442 17. Ross-Innes, C.S. *et al.* Whole-genome sequencing provides new insights into the  
443 clonal architecture of Barrett's esophagus and esophageal adenocarcinoma. *Nat Genet*  
444 **47**, 1038-46 (2015).
- 445 18. Dulak, A.M. *et al.* Exome and whole-genome sequencing of esophageal  
446 adenocarcinoma identifies recurrent driver events and mutational complexity. *Nat*  
447 *Genet* **45**, 478-86 (2013).
- 448 19. Nones, K. *et al.* Genomic catastrophes frequently arise in esophageal adenocarcinoma  
449 and drive tumorigenesis. *Nat Commun* **5**, 5224 (2014).
- 450 20. Frankell, A.M. *et al.* The landscape of selection in 551 Esophageal Adenocarcinomas  
451 defines genomic biomarkers for the clinic. *bioRxiv* (2018).
- 452 21. Yates, L.R. *et al.* Subclonal diversification of primary breast cancer revealed by  
453 multiregion sequencing. *Nat Med* **21**, 751-9 (2015).
- 454 22. Rodriguez-Martin, B. *et al.* Pan-cancer analysis of whole genomes reveals driver  
455 rearrangements promoted by LINE-1 retrotransposition in human tumours. *bioRxiv*,  
456 179705 (2018).
- 457 23. Ajani, J.A. *et al.* Esophageal and esophagogastric junction cancers, version 1.2015. *J*  
458 *Natl Compr Canc Netw* **13**, 194-227 (2015).

- 459 24. Yachida, S. *et al.* Distant metastasis occurs late during the genetic evolution of  
460 pancreatic cancer. *Nature* **467**, 1114-7 (2010).
- 461 25. Sottoriva, A. *et al.* Intratumor heterogeneity in human glioblastoma reflects cancer  
462 evolutionary dynamics. *Proc Natl Acad Sci U S A* **110**, 4009-14 (2013).
- 463 26. Mariette, C. *et al.* Pattern of recurrence following complete resection of esophageal  
464 carcinoma and factors predictive of recurrent disease. *Cancer* **97**, 1616-23 (2003).
- 465 27. Alexandrov, L.B. *et al.* Signatures of mutational processes in human cancer. *Nature*  
466 **500**, 415-21 (2013).
- 467 28. Liu, D. *et al.* Mutational patterns in chemotherapy resistant muscle-invasive bladder  
468 cancer. *Nat Commun* **8**, 2193 (2017).
- 469 29. Behjati, S. *et al.* Mutational signatures of ionizing radiation in second malignancies.  
470 *Nat Commun* **7**, 12605 (2016).
- 471 30. Dentro, S.C. *et al.* Portraits of genetic intra-tumour heterogeneity and subclonal  
472 selection across cancer types. *bioRxiv* (2018).
- 473 31. Lodato, M.A. *et al.* Aging and neurodegeneration are associated with increased  
474 mutations in single human neurons. *Science* **359**, 555-559 (2018).
- 475 32. Gao, Z., Wyman, M.J., Sella, G. & Przeworski, M. Interpreting the Dependence of  
476 Mutation Rates on Age and Time. *PLoS Biol* **14**, e1002355 (2016).
- 477 33. Letouze, E. *et al.* Mutational signatures reveal the dynamic interplay of risk factors  
478 and cellular processes during liver tumorigenesis. *Nat Commun* **8**, 1315 (2017).
- 479 34. Blokzijl, F. *et al.* Tissue-specific mutation accumulation in human adult stem cells  
480 during life. *Nature* **538**, 260-264 (2016).
- 481 35. Alexandrov, L.B. *et al.* Clock-like mutational processes in human somatic cells. *Nat*  
482 *Genet* **47**, 1402-7 (2015).
- 483 36. Pienta, K.J., Robertson, B.A., Coffey, D.S. & Taichman, R.S. The cancer diaspora:  
484 Metastasis beyond the seed and soil hypothesis. *Clin Cancer Res* **19**, 5849-55 (2013).
- 485 37. Gudem, G. *et al.* The evolutionary history of lethal metastatic prostate cancer.  
486 *Nature* **520**, 353-357 (2015).
- 487 38. Foulds, L. The experimental study of tumor progression: a review. *Cancer Res* **14**,  
488 327-39 (1954).
- 489 39. Naxerova, K. *et al.* Origins of lymphatic and distant metastases in human colorectal  
490 cancer. *Science* **357**, 55-60 (2017).
- 491 40. Sottoriva, A. *et al.* A Big Bang model of human colorectal tumor growth. *Nat Genet*  
492 **47**, 209-16 (2015).
- 493 41. Sjoquist, K.M. *et al.* Survival after neoadjuvant chemotherapy or chemoradiotherapy  
494 for resectable oesophageal carcinoma: an updated meta-analysis. *Lancet Oncol* **12**,  
495 681-92 (2011).
- 496 42. Gabriel, E. *et al.* Novel Calculator to Estimate Overall Survival Benefit from  
497 Neoadjuvant Chemoradiation in Patients with Esophageal Adenocarcinoma. *J Am*  
498 *Coll Surg* **224**, 884-894 e1 (2017).
- 499 43. Burt, B.M. *et al.* Utility of Adjuvant Chemotherapy After Neoadjuvant  
500 Chemoradiation and Esophagectomy for Esophageal Cancer. *Ann Surg* **266**, 297-304  
501 (2017).
- 502 44. Pasquali, S. *et al.* Survival After Neoadjuvant and Adjuvant Treatments Compared to  
503 Surgery Alone for Resectable Esophageal Carcinoma: A Network Meta-analysis. *Ann*  
504 *Surg* **265**, 481-491 (2017).
- 505 45. Parikh, A.R. *et al.* Liquid versus tissue biopsy for detecting acquired resistance and  
506 tumor heterogeneity in gastrointestinal cancers. *Nat Med* **25**, 1415-1421 (2019).
- 507 46. Van Roy, N. *et al.* Shallow Whole Genome Sequencing on Circulating Cell-Free  
508 DNA Allows Reliable Noninvasive Copy-Number Profiling in Neuroblastoma  
509 Patients. *Clin Cancer Res* **23**, 6305-6314 (2017).



- 510 47. Hu, Z. *et al.* Quantitative evidence for early metastatic seeding in colorectal cancer.  
511 *Nat Genet* **51**, 1113-1122 (2019).  
512 48. Robinson, D.R. *et al.* Integrative clinical genomics of metastatic cancer. *Nature* **548**,  
513 297-303 (2017).  
514

515 **Figure Legends**

516 **Figure 1 Overall project strategy and study design**

517 a. Overall Strategy to identify clonal evolution in metastatic EAC. There were three main  
518 steps in this study which comprised: Clonal discovery at autopsy (see Supplementary Note  
519 High Depth Whole Genome Sequencing (50x WGS), Mutation clustering and phylogenetic  
520 tree construction, dN/dS analysis and Mutational Signature Analysis); Spatial tracking at  
521 autopsy (see Supplementary Note Shallow Whole Genome Sequencing (1x WGS) and  
522 Temporal tracking at earlier time-points (see Supplementary Note Shallow Whole Genome  
523 Sequencing (1x) for Subclone identification, Supplementary Table 12 for precise samples for  
524 plasma and Extended Data Fig. 9 for FFPE diagnostic samples). Colored circles depict clones  
525 and subclones respectively. b. Sampling Strategy at Rapid Autopsy. Areas sampled for the  
526 50x WGS part of the study are shown in blue and for 1x WGS are shown in orange. c. Study  
527 Design and Sequencing Strategy. The flow chart demonstrates the study design and how this  
528 relates to sequencing. Clonal Discovery is in blue and Clonal Tracking in orange. The sample  
529 distribution for 50x WGS and 1x WGS are shown. 50x WGS = High depth WGS (50x), 1x WGS  
530 = Shallow WGS (1x). n = number of cases, s = number of samples. †=248 solid tissue  
531 samples, and 8 ctDNA at autopsy. CNA, copy number alteration; SNV, single nucleotide  
532 variant; MRCA, most recent common ancestor.

533 **Figure 2 Phylogenetic Analysis of ten cases with nodal and distant metastases**

534 Patient body maps (S=surgical case, P=rapid autopsy) are shown. Green circles denote  
535 lymph node metastases and yellow circles distant metastases. The labels within each circle  
536 describe the specific location (see Supplementary Table 3, 4). An organ is shown in color if  
537 metastases were sequenced from that site. The adjacent wedged semi-circle depicts the  
538 clinical timelines for each patient. Each wedge corresponds to one month; blue wedges  
539 indicate the total lifetime of the patient and red wedges periods of therapy. Phylogenetic  
540 trees for each patient are shown and methodology is in Supplementary Note and Extended  
541 Data Fig. 1a-b; pink = truncal events shared by all samples, purple = branch events shared by  
542 more than one sample, yellow = leaves, events unique to a sample. The circle at the end of  
543 a trunk, branch or leaf represents a clone or subclone. Each clone or subclone is annotated  
544 to show which samples it is present in. E1-E4 = primary esophageal tumor, L1-L4= lymph  
545 nodes, D1-8 =distant metastases, B = Barrett's Esophagus. A subclone annotated with E1, L2

546 for example indicates that this subclone is seen only in samples E1 and L2. The CCF of each  
547 subclone/clone (barring the MRCA) is in Supplementary Table 5 and 6. The length of the  
548 branches of the tree are reflective of the number of SNVs in the subclone/clone. The scales  
549 adjacent to each case are relative, given the variable number of SNVs per case. Trees are  
550 annotated with potential driver events, black: missense variants, red: amplifications. Gray  
551 dots outlined with a black dashed line denote the first subclone/clone to metastasize that  
552 would be classified as non-curative based on anatomical location. Red dots mark the  
553 stellate pattern on the phylogenetic tree.

### 554 **Figure 3 Mutational Signatures**

555 a. Contributions of mutational signature in 18 cases (n=122) across the cohort. The bar chart  
556 displays samples on a per case basis (X-axis) and depicts the number of SNVs contributing to  
557 each signature (Y-axis). b. Mutational signatures pre-and post- diaspora across all samples  
558 (n=122) in 18 cases.

559 Mutations were separately assigned to signatures and the proportion of mutations within  
560 each case assigned to each signature is shown. Dark lines = median, Boxes = 25th and 75th  
561 quartiles, whiskers extend to the most extreme point within 1.5× interquartile range of the  
562 box edge. Signatures 1 mutations have a significantly lower representation in post-diaspora  
563 mutations, while signature 3 mutations have significantly high. c. Mutational signature  
564 analysis of ageing signature (signature 1) pre-and post-diaspora in all cases (n=8) with local  
565 and distant spread ( $p < 1.18 \times 10^{-90}$  across all cases) Chi squared test was used to determine  
566 the p value. Survival is shown in months from the point of diagnosis \*=cases which  
567 underwent surgery.

568

### 569 **Figure 4 1x WGS and similarity matrix clustering of 248 further tissue samples from six** 570 **cases**

571 1x WGS was performed at an average depth of 1x to track subclones and clones previously  
572 discovered using 50x WGS for further tissue samples (n=248). Pearson correlation  
573 similarity matrix clustering was performed on all samples for each case (plotted against  
574 each other) with red indicating sample similarity ( $r=1$ ) and blue indicating dissimilarity ( $r=-$   
575  $1$ ). Sample sites used in this part of the study are shown in Supplementary Table 9 and the  
576 entire organ is highlighted if solid organ sites were sequenced. For example, liver  
577 metastases were only seen in P4, P6, P8, P10. Similarly, P2 had lymph nodes only (only

578 colored dots are seen which represent lymph nodes, no solid organs are highlighted).  
579 Clustering was performed based on the presence of subclones and clones already  
580 detected using 50x WGS and distinct clusters were identified for each case as  
581 demonstrated by the adjacent key per case (each group is both colored and numbered).  
582 Samples are displayed on the adjoining body maps for which the color coding corresponds  
583 to the genomic clustering in the adjacent heatmap. Sites with multiple samples are  
584 magnified and the division of samples shown. Maps of the primary tumor with  
585 representation of metastatic subclones are shown with each case, with the colors of the  
586 subclones being the same as those in the matrix and body map. Areas shaded red in the  
587 primary tumor represent subclones that were not detected in the metastatic samples that  
588 underwent 1x WGS and were instead confined to areas of the primary tumor.

589

#### 590 **Figure 5 Temporal and spatial tracing of metastatic subclones in plasma**

591 a. Plasma ctDNA 1x WGS and digital droplet PCR (ddPCR) analysis for *TP53* mutant allele  
592 fraction (MAF) for P10 and P6. The MAF of *TP53* (%) is shown on the Y-axis and days from  
593 diagnosis are shown on the X-axis. The shaded areas represent time periods of therapy. 1x  
594 WGS at select time-points was performed and the clonal composition of these samples  
595 are shown by the presence of colored clusters. The color of each corresponds to the color  
596 of the corresponding node on the adjacent 50x phylogenetic tree with the presence of  
597 colored clusters which correlate with the 50x tree. Moreover, copy number traces for  
598 each time point are shown for select chromosomes. b. The presence or absence of  
599 amplifications and deletions in plasma compared to tissue, detected from 1x WGS for 8  
600 cases. Tissue refers to all samples collected at autopsy and at earlier time-points. c.  
601 Stacked bar charts to demonstrate the presence or absence of clusters across all plasma  
602 samples, including truncal and branch clusters using 1x WGS.

603

#### 604 **Figure 6 Diaspora model of metastatic spread and associated features**

605 Panel a depicts clonal diaspora with colored circles representing clones and subclones. \*=  
606 evidence of selection. Panel b explains the five features seen in diaspora (one is defining,  
607 and the other are associated with diaspora) and whether these are present (✓) or absent  
608 (x) in each case. \*✓ implies that the feature is present, and that the evidence was from  
609 1x WGS.

## 610 **Methods**

### 611 **Statistics**

612 Unless otherwise stated, statistical analyses were performed using R, version 3.3.3.  
613 Clustering of mutations was carried out using a previously published Bayesian Dirichlet  
614 Process method, DPCLust (<https://github.com/Wedge-Oxford/dpclust>), which calculates  
615 CCFs of each SNV, taking into account tumor purity and copy number aberrations as  
616 previously described<sup>49</sup>. Analysis of structural variants used generalized linear models,  
617 implemented with the R package MASS. Grouping of 1x WGS samples was performed with  
618 the GENE-E package (<https://software.broadinstitute.org/GENE-E/download.html>).  
619 Wilcoxon signed rank tests and Chi-squared tests were used as described in the main text.  
620 Simulations were used to ascertain the robustness of DPCLust to violations of the infinite  
621 sites assumption and its sensitivity to detect small deviations from stellate patterns.  
622 Simulations were also used to confirm the correlation between the number of mutations  
623 detected from 1x WGS and CCF determined from 50x WGS, as described in Online Methods.  
624 dN/dS analysis was performed using the previously published package dndscv<sup>50</sup>  
625 (<https://github.com/im3sanger/dndscv>).

626

### 627 **Patient recruitment and Sample collection**

628 EAC patients were recruited from Addenbrooke's Hospital, Cambridge University Hospitals  
629 NHS Trust with the explicit aim to study the clonal evolution of metastases as a sub-study  
630 within OCCAMS (Oesophageal Clinical And Molecular Stratification). When it was clear that  
631 extensive sampling of metastases could not be achieved without multiple invasive  
632 procedures, the PHOENIX autopsy study was set up (Phylogenetic of Oesophageal  
633 Neoplasia – An Investigation of Clonal Expansion under REC 07/H0305/52, and REC  
634 EE/0043) with a prospective study design. Due diligence was undertaken to ensure  
635 compliance with ethical regulations at all times. Patients were eligible if they were at least  
636 18 years of age and had received a confirmed diagnosis of EAC following central pathology  
637 review. Patients were only approached for the PHOENIX study following a palliative  
638 diagnosis of metastatic EAC, with the full involvement of the multidisciplinary team.  
639 Samples from the PHOENIX autopsy study were obtained within 6 hours of death and all  
640 post-mortems were carried out at Papworth Hospital NHS Trust, United Kingdom.

641 Samples from Cambridge OCCAMS patients were obtained during diagnostic  
642 oesophagogastroduodenoscopy (OGD), at endoscopic ultrasound (EUS) and/or from the  
643 surgical resection specimen. Where possible, multiple samples were taken from spatially  
644 distinct sites of the primary tumor or metastases. In two cases, brain metastases were  
645 sampled at a clinically indicated craniotomy. Blood or normal squamous esophageal  
646 samples, at least 5cm distant from the tumor, were used as a germline reference.

647 All tissue samples were snap-frozen in liquid nitrogen immediately after collection and  
648 stored at -80°C. Cancer samples were deemed suitable for DNA extraction only after  
649 consensus review of an H&E stained frozen section, from the same sample that would be  
650 sent for sequencing, by two expert pathologists who confirmed tumor cellularity at  $\geq 70\%$ .

651 Samples with overall  $\geq 70\%$  cellularity underwent dissection of the whole surface area with  
652 a scalpel, whereas marked areas of  $< 70\%$  underwent macrodissection or laser capture  
653 micro- dissection aided by methylene blue staining visualized on the PALM-Zeiss  
654 microscope (Zeiss, Oberkochen, Germany). An H&E stained slide was obtained before and  
655 after extraction to confirm tumor cellularity of the microdissected section.

656 DNA was extracted from frozen tissues using the All PrepDNA/RNA Mini Kit (Qiagen,  
657 Hilden, Germany) and from blood samples using the Nucleon™ Genomic Extraction kit  
658 (Gen-Probe, San Diego, USA) according to the manufacturer's instructions. Some samples  
659 were preserved in paraffin blocks after initially being stored in formalin. DNA from these  
660 samples was extracted using the QiAmp FFPE Kit (Qiagen). Plasma extraction (for ctDNA)  
661 was performed using the QiASymphony platform (Qiagen) as per the manufacturer's  
662 instructions. All samples were eluted in 60µl of AE buffer and quantified using the High  
663 Sensitivity Qubit (Thermo Fisher Scientific, MA, USA).

664 We included 388 samples, predominantly from PHOENIX, and some additional samples  
665 from surgery and endoscopy (part of esophageal ICGC).

666 All samples were collected according to a strict SOP with quality control measures as already  
667 described. All demographic and clinical data was anonymized and stored on a central study  
668 database (OpenClinica and Labkey). The clinical characteristics of the patients are provided  
669 in Supplementary Table 1 and 2. In terms of specifics of sample collection at autopsy, the  
670 primary tumor was opened down the midline of the esophagus and the greater curve of the  
671 stomach to expose the lumen. The tumor was divided in 12 areas with sampling as shown.

672 The size of tumors varied per case, but the division of sampling was always kept identical to  
673 preserve reproducibility. In terms of the strategy for genomic sequencing (as per Figure 1),  
674 up to 3 lymph nodes were chosen for 50x WGS in the areas shown (cervical, regional and  
675 para-aortic) and up to 24 lymph nodes in each case (8 further lymph nodes per cervical,  
676 regional and para- aortic areas (as per the Japanese Classification of nodal staging<sup>51</sup>) were  
677 chosen for the 1x WGS part of the study. At least one metastasis per solid organ was chosen  
678 for 50x WGS and for the 1x WGS part up to 8 samples were taken per organ for further  
679 analysis. In addition, 8 samples from metastatic sites which had previously been sequenced  
680 for 50x WGS were further sequenced for 1x WGS to assess the effects of metastatic  
681 heterogeneity.

682

### 683 **Whole genome sequencing and data analysis strategy**

684 We used the Illumina HiSeq platform to perform WGS on multiple regions collected from  
685 each primary tumor, lymph node and/or solid organ metastasis (Figure 1a,b, Supplementary  
686 Table 3, 4). All DNA extractions and WGS conformed with ICGC quality control standards and  
687 required  $\geq 70\%$  cellularity and a matched germline sample. WGS was performed at high  
688 depth (median coverage 66.3, IQR 56.1-87.2) to discover mutations in 122 samples from 18  
689 patients (Supplementary Table 3, 4). In addition, low depth WGS (median coverage 1, IQR 1-  
690 5) was performed to track these mutations spatially in up to 48 solid tissue samples per  
691 case, (total=248) and 8 ctDNA samples at autopsy. Temporal tracking was performed in  
692 cases with archival biopsy material, and where historical bloods were available  
693 (Supplementary Table 12, Figure 5, Extended Data Fig. 6). For each patient the number of  
694 subclones and the cancer cell fraction within each subclone was inferred using an extension  
695 of a previously described Bayesian Dirichlet process<sup>11</sup> and we applied a set of previously  
696 described rules to derive a phylogenetic tree (Additional Methods<sup>52</sup>). All sequencing data  
697 have been deposited in the European Genome-Phenome Archive under accession number  
698 EGAD00001005434. *TP53* analysis in cell free tumor DNA (ctDNA) was performed using  
699 Digital PCR on the Bio-rad platform (Bio-rad, California) using validated *TP53* assays  
700 (Supplementary Table 14).

701

## 702 **Mutation clustering and phylogenetic tree construction**

703 The workflow used to perform mutation clustering and phylogenetic tree construction is  
704 depicted in Extended Data Fig. 1a and illustrated with an example case, S3, in Extended  
705 Data Fig. 1b. For each patient, we inferred the number of subclones and the fraction of  
706 tumor cells within each subclone by using a previously described Bayesian Dirichlet process  
707 (BDP) to cluster mutations according to their mutation copy number<sup>49</sup>. We extended this  
708 process into  $n$  dimensions for patients with  $n$  related samples, where the number of  
709 mutant reads obtained from multiple related samples were modelled as independent  
710 binomial distributions. The BDP uses Markov chain Monte Carlo (MCMC) to sample the CCF  
711 values of the subclones in each sample. MCMC is run for 1000 iterations and outputs, for  
712 each iteration, the sampled position of each cluster,  $p_{i_h}$  and the weight of each cluster,  $V_h$ ,  
713 which is an estimate of the proportion of mutations assigned to that cluster. The first 200  
714 iterations are considered as a ‘burn-in’ and are not used in subsequent steps. In order to  
715 obtain the set of subclones present within a tumor and their CCF values, the following  
716 procedure was followed:

- 717 • Using the aforementioned MCMC sampling of CCF values from all  $n$  samples, for  
718 every possible triplet of samples, obtain posterior density estimates of CCF using  
719 the function `kde` in the R package `ks`, with input parameters  $x = p_{i_h}$ , `bandwidth =`  
720 `0.1`, `w = V_h`. Set `gridsize` such that density estimates are obtained to a resolution of  
721 `0.02`. Identify local peaks in the posterior mutation density as locations higher  
722 than any other gridpoint within a range of 2 gridpoints. For each local peak, define  
723 a region representing a ‘basin of attraction’, defined by a set of planes running  
724 through the `_point` of minimum density between each pair of cluster positions.  
725 Assign each mutation to the cluster in whose basin of attraction they are most  
726 likely to fall, using CCF values from MCMC sampling.
- 727 • Across the set of all possible triplets, identify sets of mutations that are assigned  
728 to the same cluster in every triplet. Estimate the CCF of each cluster as the mean  
729 CCF of the mutations assigned to that cluster. Estimate the 95% confidence  
730 intervals as the `[0.025,0.975]` quantiles of the mean  $p_{i_h}$  values of the mutations  
731 assigned to each cluster within MCMC sampling.

732 Finally, again using the aforementioned MCMC sampling of CCF values from all  $n$  samples,  
733 for every pair of samples, plot the mutation density, estimated using the function `kde` in



734 the R package *ks*, with input parameters  $x = \pi_{i_h}$ , bandwidth = 0.1,  $w = V_{i_h}$ .

735 Taking a conservative approach, clusters were identified as subclonal only if the 95%  
736 confidence intervals of the posterior estimate of the proportion of cells excluded the value  
737 1. Clusters containing less than 1% of all mutations identified in a tumor were not included  
738 in phylogenetic reconstruction.

739 Occasionally, copy number states are incorrectly called in small regions of some cancer  
740 genomes. As a consequence, mutations falling in these regions have inaccurate estimates  
741 of CCF and can cause artefact clusters. Such clusters may be identified after mutation  
742 clustering since they contain a small percentage of mutations (less than 2.5%), the  
743 mutations within them are located in localized regions of the genome, and, often, they  
744 cannot be placed on the phylogenetic tree because they have discordant CCF values. We  
745 excluded these clusters from phylogenetic tree construction. The number of clusters  
746 excluded in total was seven (5 in P2, 1 in P3, 1 in P10). Two samples had low tumor content  
747 (36% in P3\_E1, 14% in S5\_T1). As a result, CCF estimates for subclones found in these  
748 samples are imprecise and led to violations of the sum rule (see below). The CCF values of  
749 the relevant clusters were manually corrected to enable them to be placed on the  
750 phylogenetic tree, as follows: P3\_E1 only cluster adjusted from 1 to 0.85; S5\_E1 truncal  
751 cluster adjusted from 0.85 to 1.

752 To determine the most likely phylogenetic tree, we applied two rules, previously  
753 described<sup>52</sup>. Briefly, the ‘sum rule’ (which is an extension of the pigeonhole principle  
754 described in Ref 11), asserts that if a subclone A is ancestral to both subclones B and C and  
755 if the summed CCFs of B and C exceed the CCF of A in any sample, the relationship  
756 between the subclones must be linear. The ‘crossing rule’ is applied to tree construction  
757 from multiple samples. It asserts that if the CCF of B is higher than the CCF of C in sample X  
758 and the CCF of B is lower than the CCF of sample C in sample Y then B and C must be in  
759 separate branches of the phylogenetic tree, i.e. they are not collinear. For all clonally  
760 related samples, the same underlying phylogenetic tree must exist. This exerts much  
761 greater stringency to the inferred ordering of subclonal clusters present in more than one  
762 sample and defines their position on the phylogenetic tree unequivocally. Note that P9  
763 contains two independent cancers derived from Barrett’s esophagus and adenocarcinoma  
764 regions. CCF values are reported relative to the dominant cancer, so in P9\_D4, which  
765 contains both cancers, the two cancers are reported with CCFs of 100% and 69%. This

766 apparent violation of the sum rule results from the mathematical convenience of  
767 normalizing to the dominant cancer.

768 It should be noted that the sum rule and crossing rule only strictly apply when the infinite  
769 sites assumption (ISA) is obeyed. The ISA states that each mutation only occurs once during  
770 the lifetime of a tumor and that mutations never revert to normal. A recent study<sup>53</sup> has  
771 shown, through analysis of targeted sequencing of single cells, that the ISA is not always  
772 followed in real data, for two reasons:

- 773 • Copy number alterations (CNAs), specifically losses and loss of heterozygosity,  
774 have the effect of removing mutations in the deleted region, resulting in the  
775 apparent 'reversion' of a mutation.
- 776 • The same mutation may occur on more than one occasion, particularly if the  
777 mutation is a driver mutation.

778 In our study, we take account of CNAs when calculating the CCF of each mutation. In  
779 regions that have undergone gain of one or both alleles, a mutation may be present on  
780 more than one chromosome copy, up to the number of copies of the most amplified  
781 chromosome copy. Conversely, if one or both chromosome copies have undergone loss in  
782 a particular sample, a mutation may be lost in that sample. In the situation where a  
783 mutation is unobserved in a sample and that sample has a copy number state lower than  
784 that observed in another sample in which the mutation is observed, we do not call the  
785 mutation as absent. Rather, we cluster it based on its CCF in the remaining samples,  
786 treating its CCF in the target sample as unknown.

787

#### 788 **Identification of cancer cell fraction**

789 For each mutation we calculated the mutation copy number as previously described, using  
790 the mutant allele burden, tumor cellularity and locus specific copy number in the tumor  
791 and matched normal<sup>49</sup>. The mutation copy number reflects the percentage of tumor cells  
792 within a sample carrying that mutation, and permits the cross-comparison of the mutation  
793 in related samples despite differences in tumor purity and/ or copy number profiles.  
794 Mutations present on multiple copies of a chromosomal segment will have a mutation  
795 copy number greater than 1. To group mutations according to the percentage of cells  
796 containing it, or cancer cell fraction (CCF), the number of chromosomes carrying the  
797 mutation must be determined. For all mutations within amplified regions with a major

798 allele copy number, the observed fraction of mutated reads was compared to the expected  
799 fraction of mutated reads resulting from a mutation present assuming a binomial  
800 distribution<sup>37</sup>.

801

## 802 **Annotation of the trees with mutations**

803 We annotated each tree with oncogenic or putative oncogenic alterations including  
804 substitutions and copy number changes. For substitutions, cluster assignment information  
805 from a multidimensional Dirichlet process was used.

806 For rearrangements and copy number changes, branch assignment was achieved by  
807 considering the set of samples containing the variant and the subclonal fraction of the  
808 associated copy number segment where applicable. All potential driver alterations were  
809 annotated. For substitutions, structural variants and copy number events, these included a  
810 set of genes compiled from the TARGET database from the Broad Institute and multiple  
811 sequencing datasets for OAC<sup>14-16,18,19</sup>.

812

## 813 **Shallow Whole Genome Sequencing for Subclone Identification**

814 For shallow whole genome sequencing, samples were sequenced to a median depth of  
815 ~1x. It was not therefore feasible to call mutations de novo for these samples, but we were  
816 able to count the number of mutations from each subclone that reported a mutant read in  
817 1x WGS sequencing. We performed simulations of 1x WGS data in order to ascertain the  
818 correlation between the number of mutations identified and the CCF of each subclone.  
819 First, we simulated subclones with CCF values between 0.01 and 1.00, assuming 1000  
820 mutations per subclone, sequencing depth drawn from a Poisson distribution with  
821 expected value 1, and binomial sampling of WT and mutant reads. The correlation  
822 between the number of mutations detected and the CCF of the subclone was very high  
823 (Pearson  $r = 0.992$ , Extended Data Fig. 4). In order to test whether subclones containing  
824 fewer mutations also had good correlations between CCF and number of detected  
825 mutations, we performed further simulations of subclones containing between 50 and  
826 1,000 mutations and ascertained that the correlation remained very high ( $> 0.997$ ) for  
827 cluster sizes as small as 200 (Extended Data Fig. 5). Of the 169 subclones identified in our  
828 study, only two contained fewer than 200 mutations, indicating that the number of

829 mutations detected is a good proxy for the CCF of a subclone.  
830 SNVs from libraries sequenced to a minimum of 1x following filtering, were allocated to  
831 subclones previously identified at 50x WGS. Mapping quality and base quality of 10 were  
832 used. This resulted in tabulated counts for SNVs being allocated to subclones identified at  
833 50x WGS for each sample. Normalization was performed according to the number of SNVs  
834 assigned to each subclone from 50x WGS, and to the total number of SNVs in that sample  
835 in order to account for potential differences in coverage, using the following equation:

$$836 \text{CCF}_{\text{cluster}} = n_{\text{cluster}}/n_{\text{truncal}} \times H_{\text{truncal}}/H_{\text{cluster}}$$

837 in which  $n_{\text{cluster}}$  and  $n_{\text{truncal}}$  are the numbers of loci in the target cluster and the truncal  
838 cluster that have mutant reads in the target sample and  $H_{\text{cluster}}$  and  $H_{\text{truncal}}$  are the number  
839 of mutations identified from 50x WGS in the target and truncal clusters. For each 1x WGS  
840 sample, this provides an estimate of the CCF of each subclone within that sample.

841 In all cases, near equal coverage was obtained and in cases of low cellularity further  
842 sequencing was performed in order to achieve this. After normalization, the GENE-E  
843 package (<https://software.broadinstitute.org/GENE-E/download.html>) was used to cluster  
844 the 1x WGS samples according to the similarity of their CCF profiles using Pearson  
845 correlation.

846

#### 847 **Data Availability**

848 Sequencing data that support the findings of this paper have been deposited in the  
849 European Genome-phenome Archive with the accession code EGAD00001005434.

850

#### 851 **Code Availability**

852 All code required to reproduce the analysis outline in this manuscript can be found in the  
853 main and supplementary methods. There are no restrictions to the accessibility of this code.

854

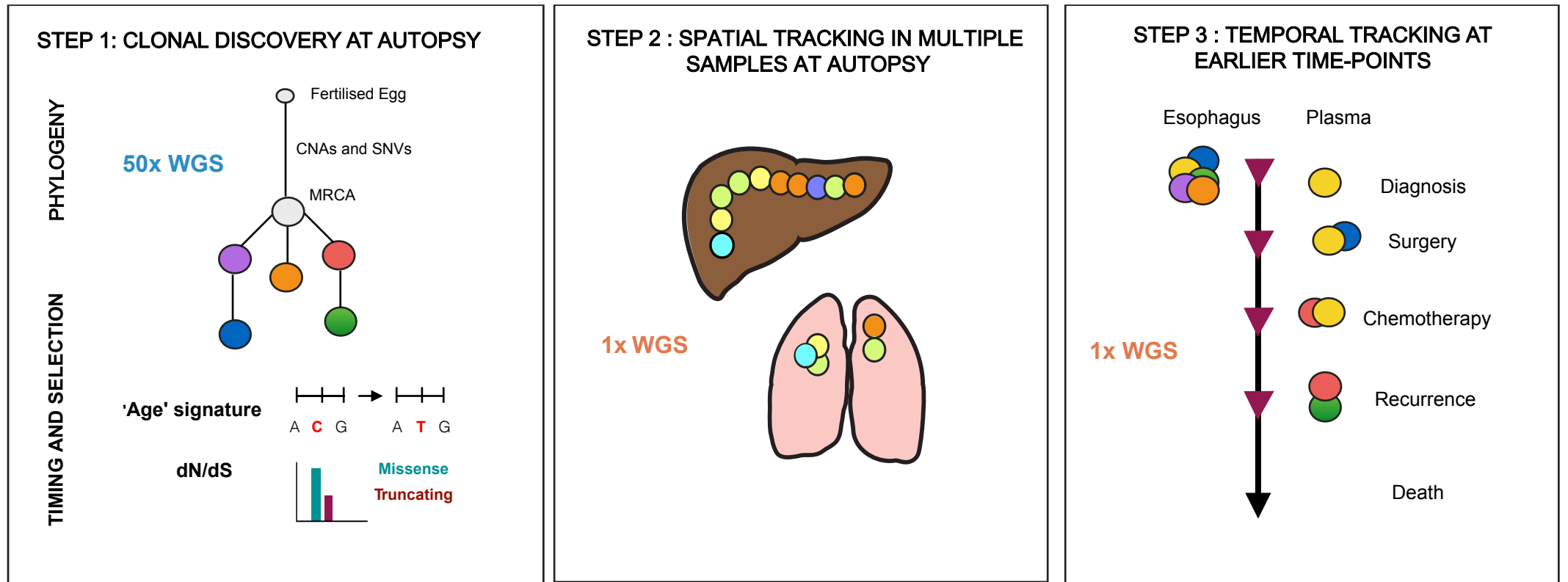
#### 855 **Method-only references**

- 856 49. Bolli, N. *et al.* Heterogeneity of genomic evolution and mutational profiles in multiple  
857 myeloma. *Nat Commun* **5**, 2997 (2014).  
858 50. Martincorena Inigo, R.K.M., Gerstung Moritz, Dawson Kevin J, Haase Kerstin, Van  
859 Loo Peter, Davies Helen, Michael R. Stratton Michael R, Campbell Peter J. Universal  
860 Patterns Of Selection In Cancer And Somatic Tissues. *Cell* (2017).  
861 51. Japanese Gastric Cancer, A. Japanese classification of gastric carcinoma: 3rd English  
862 edition. *Gastric Cancer* **14**, 101-12 (2011).

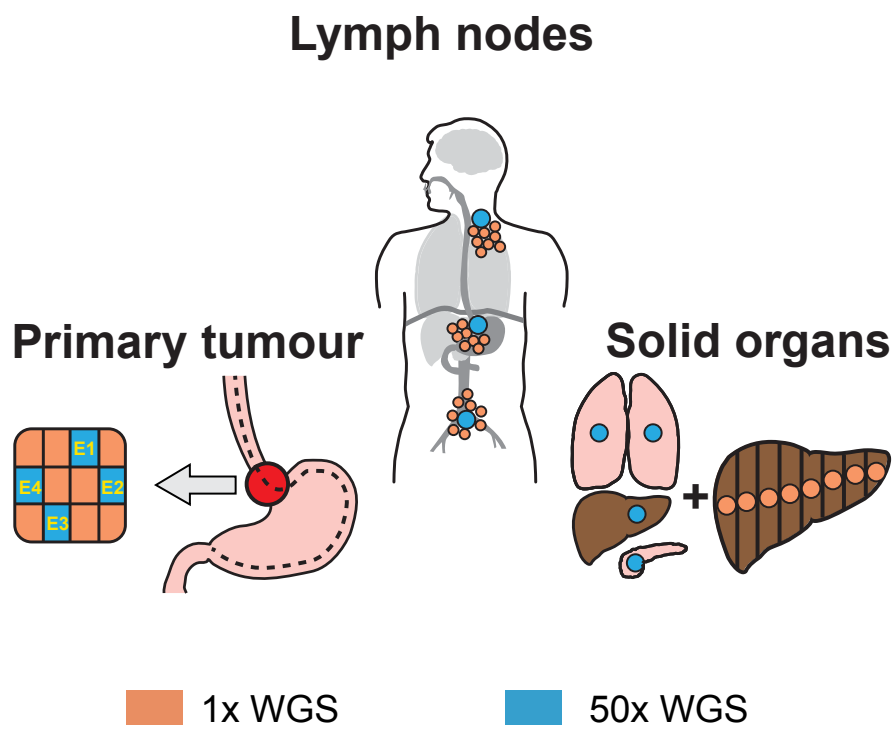
- 863 52. Jiao, W., Vembu, S., Deshwar, A.G., Stein, L. & Morris, Q. Inferring clonal evolution  
864 of tumors from single nucleotide somatic mutations. *BMC Bioinformatics* **15**, 35  
865 (2014).
- 866 53. Kuipers, J., Jahn, K., Raphael, B.J. & Beerenwinkel, N. Single-cell sequencing data  
867 reveal widespread recurrence and loss of mutational hits in the life histories of tumors.  
868 *Genome Res* **27**, 1885-1894 (2017).  
869

Figure 1

a OVERALL STRATEGY TO IDENTIFY CLONAL EVOLUTION IN METASTATIC EAC



b SAMPLING STRATEGY



c SEQUENCING STRATEGY

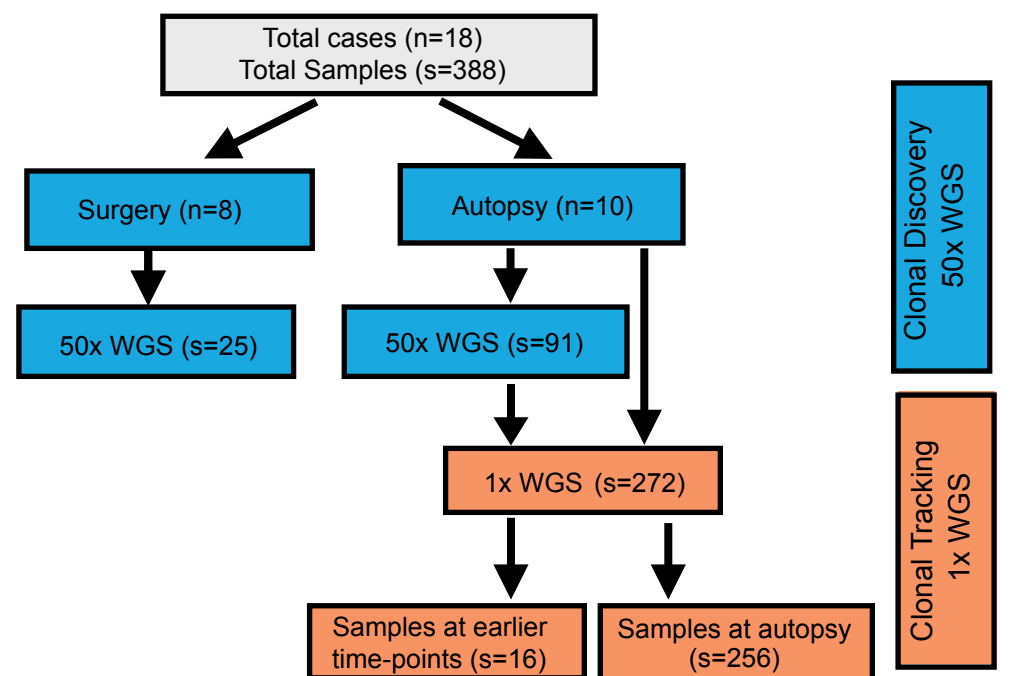


Figure 2

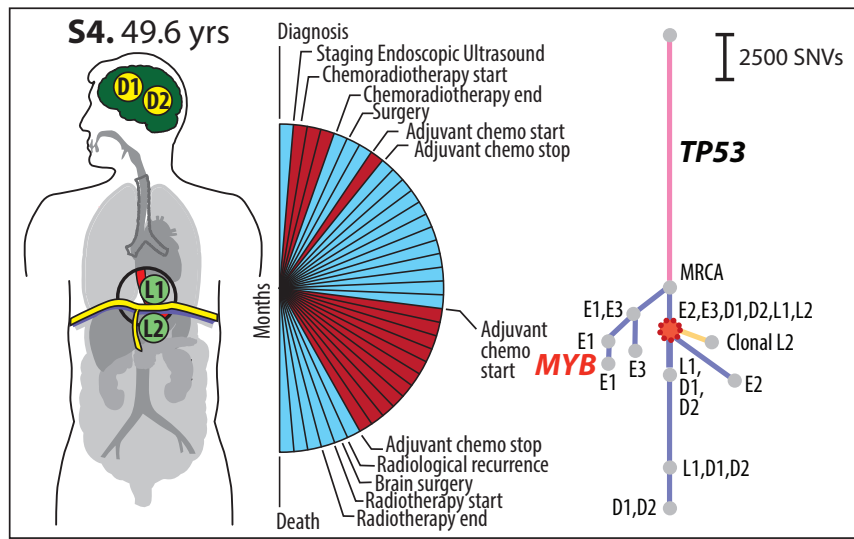
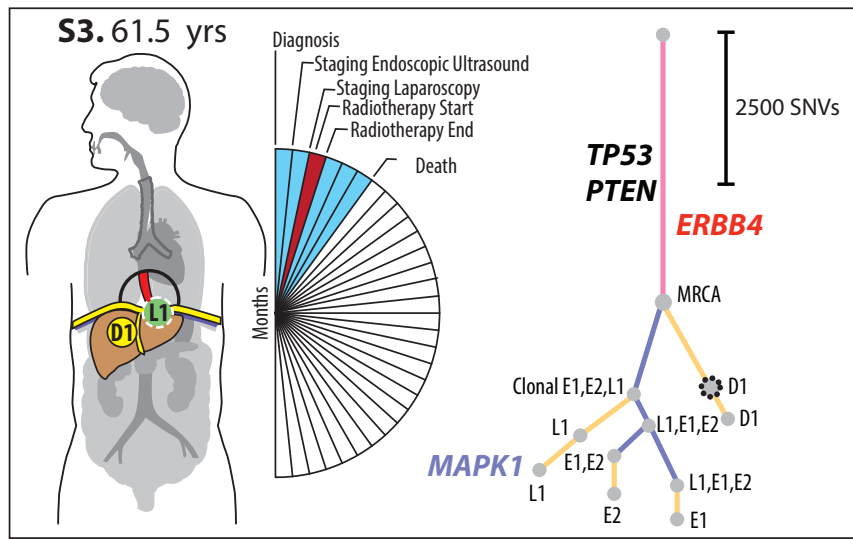
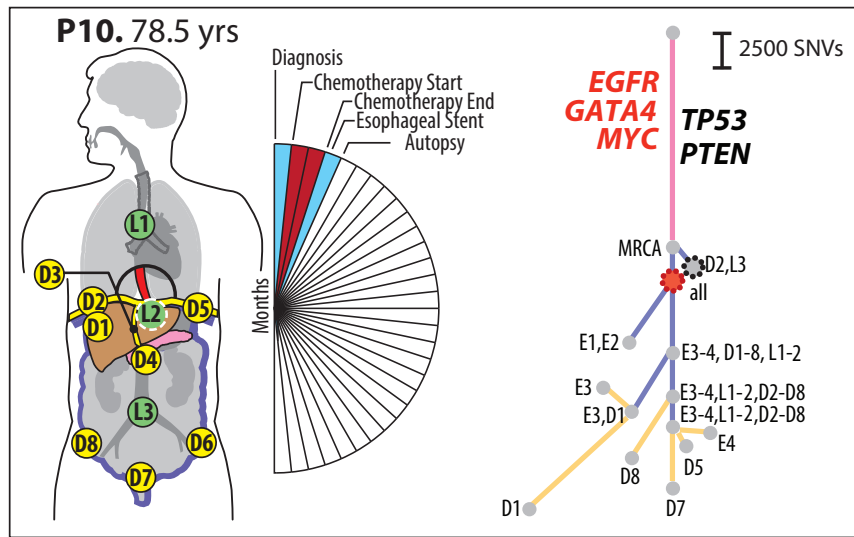
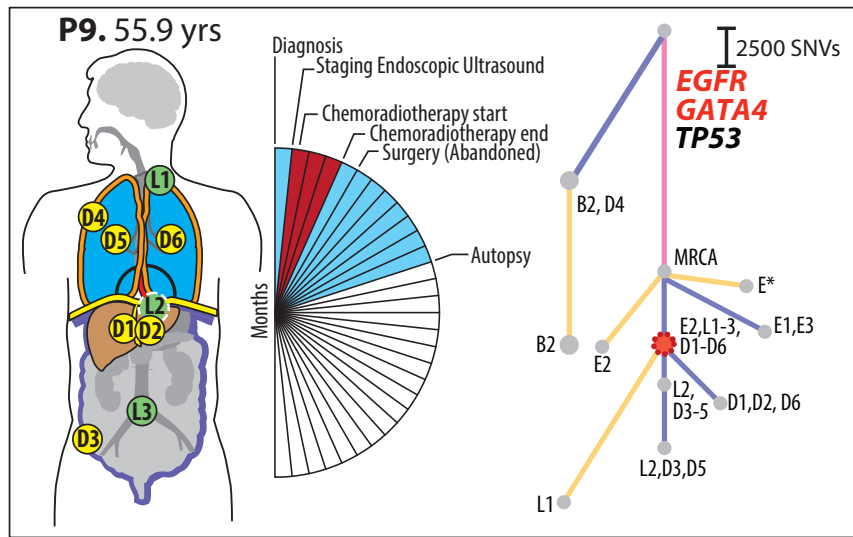
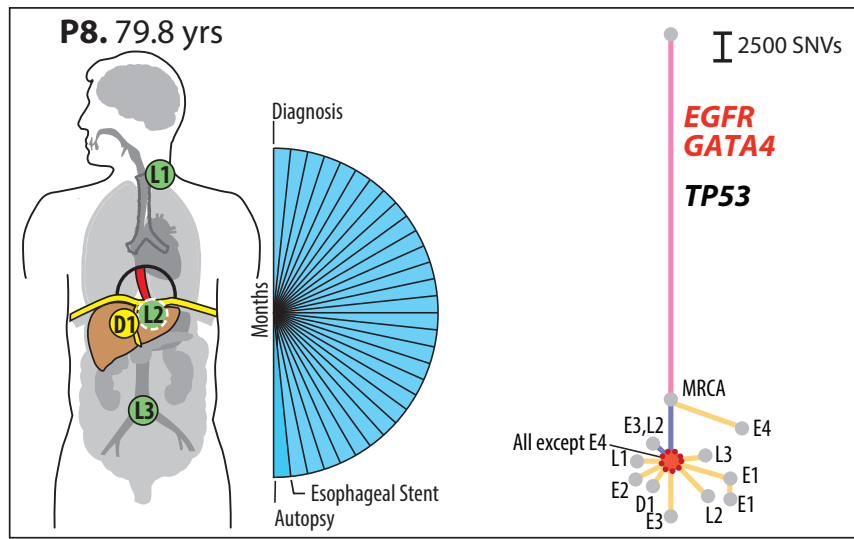
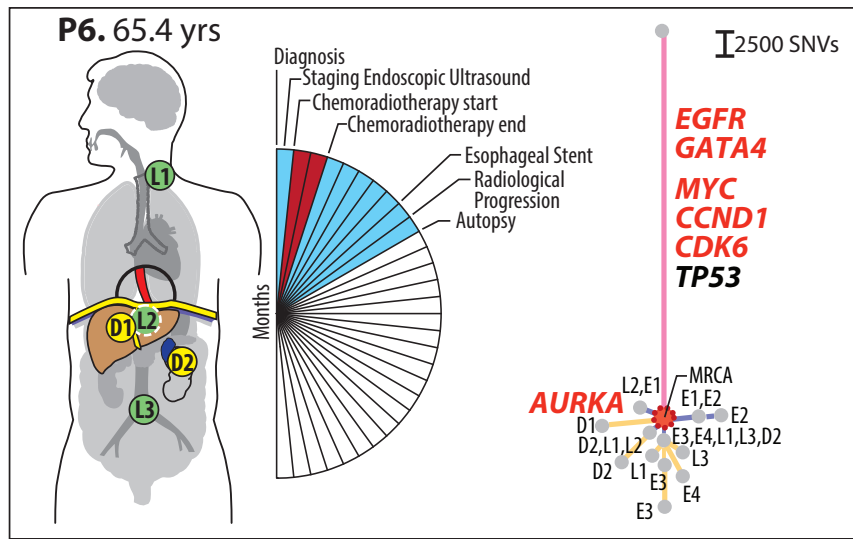
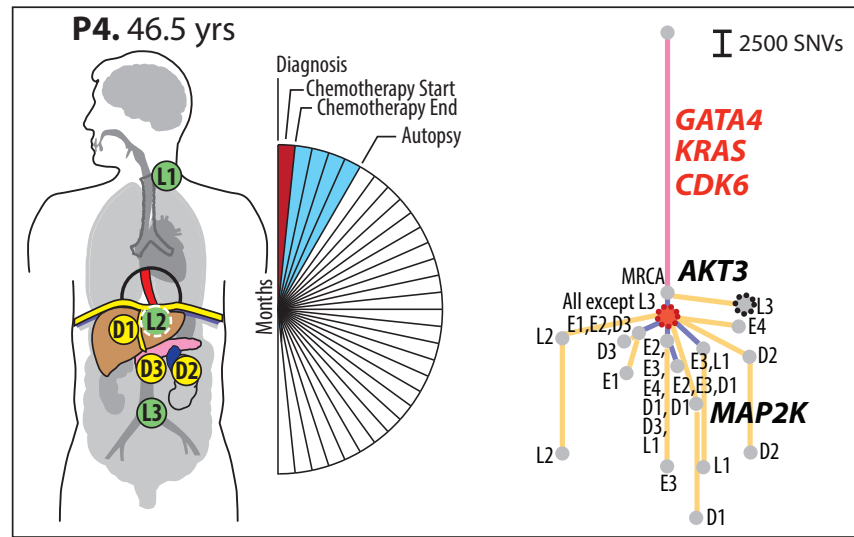
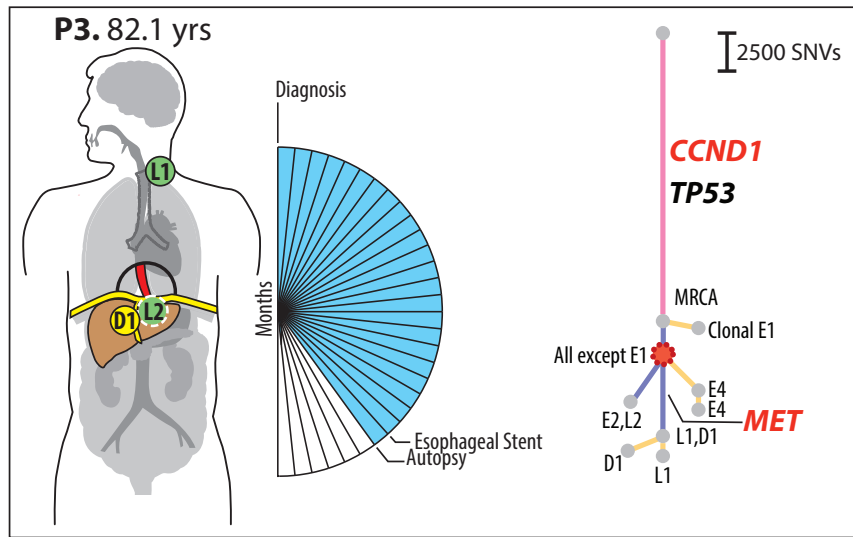
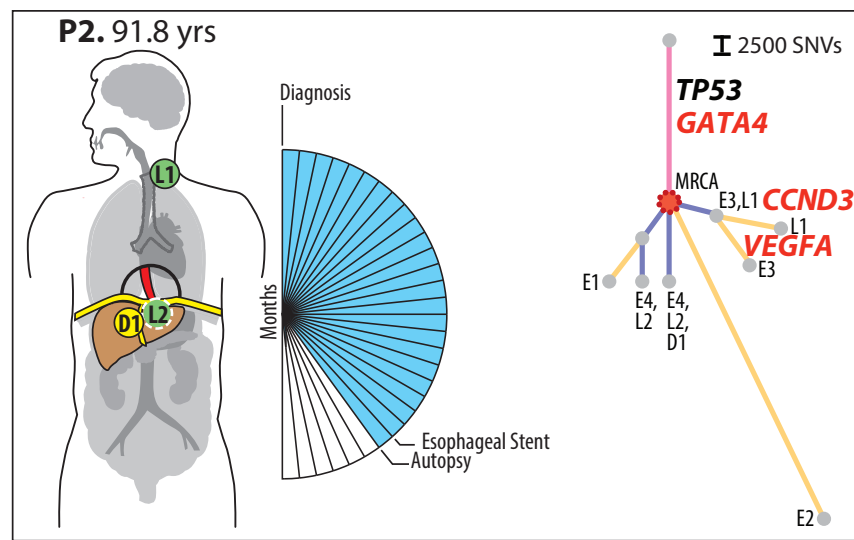
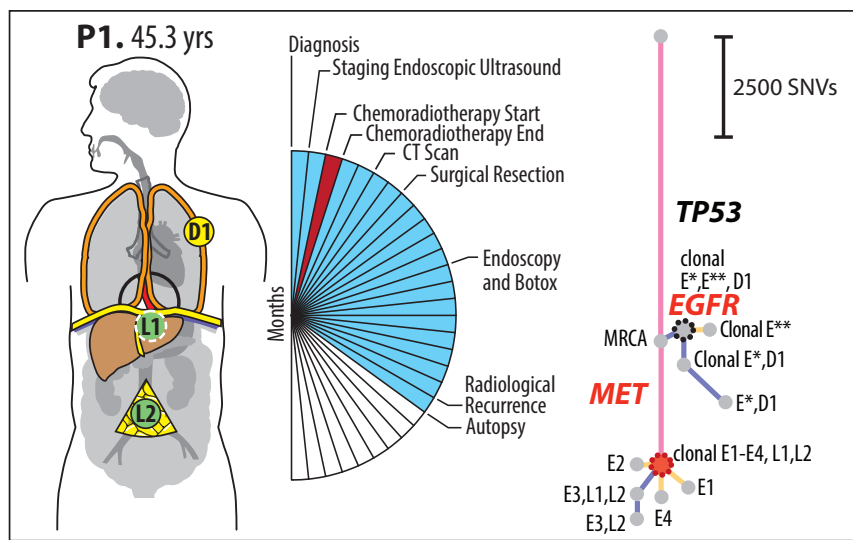
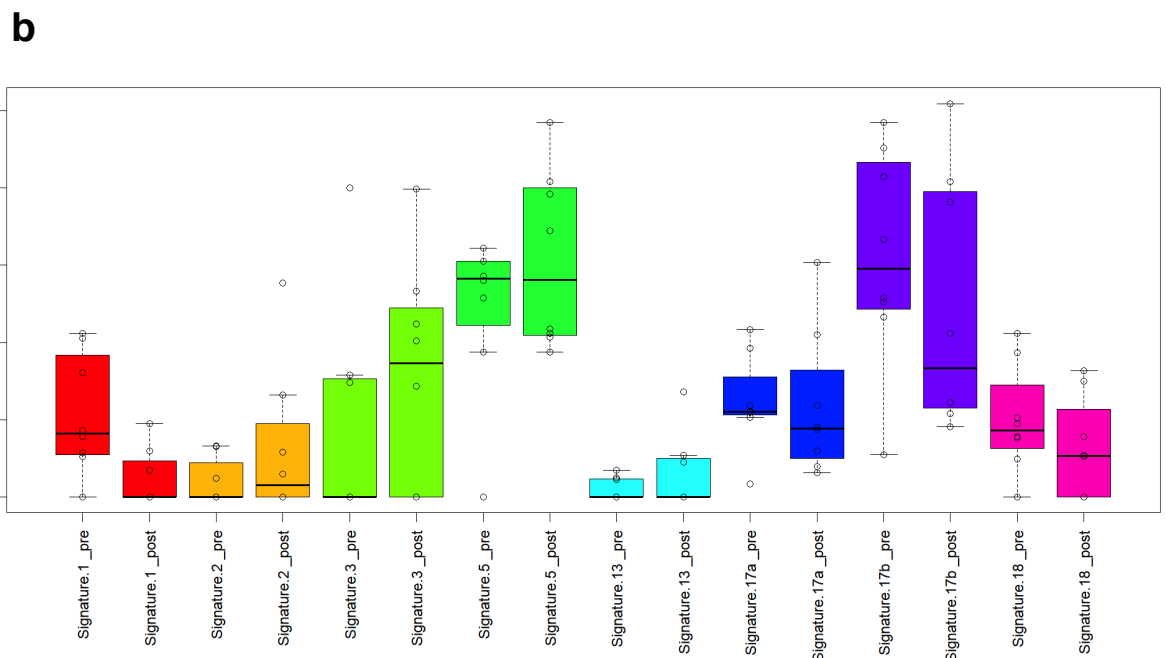
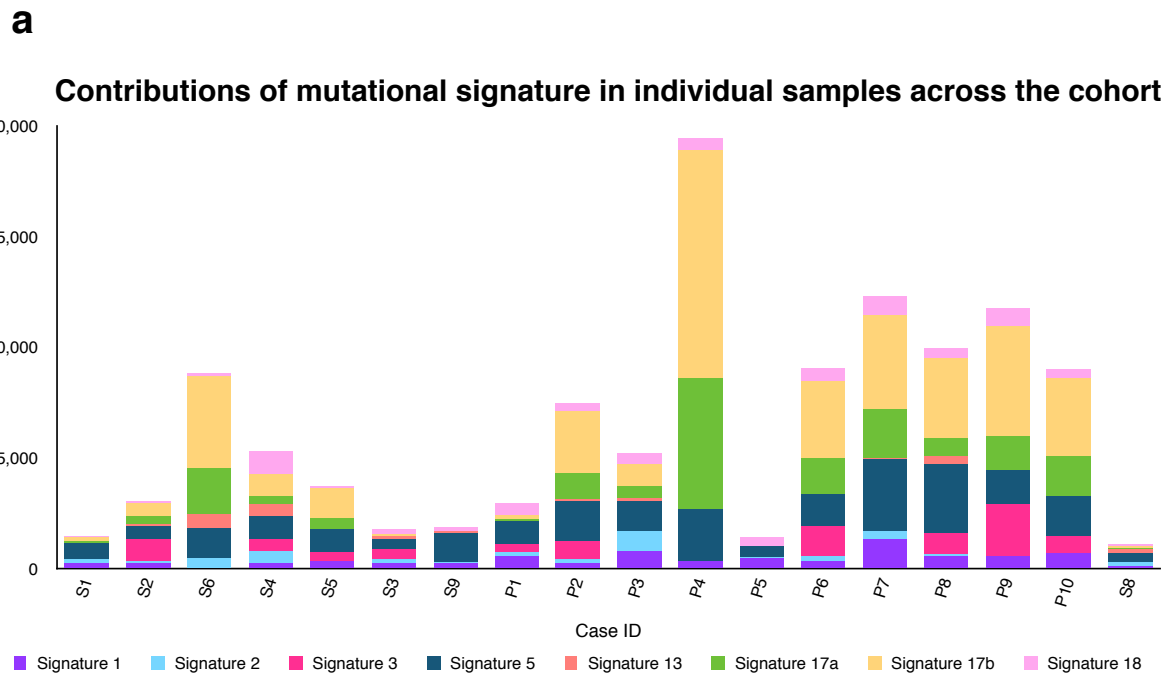


Figure 3



**c**

Case	Pre-Diaspora	Post-Diaspora	p value	Survival (months)
P1			9.10E-08	20*
P2			9.09E-05	12
P3			3.19E-05	14
P4			1.56E-95	5
P6			3.10E-14	5
P8			5.87E-38	30
P9			5.82E-72	12
P10			6.58E-161	4
S4			1.11E-14	37*

● Percentage of Clocklike  
● Signature Percentage Non-Clocklike Signature



Figure 4

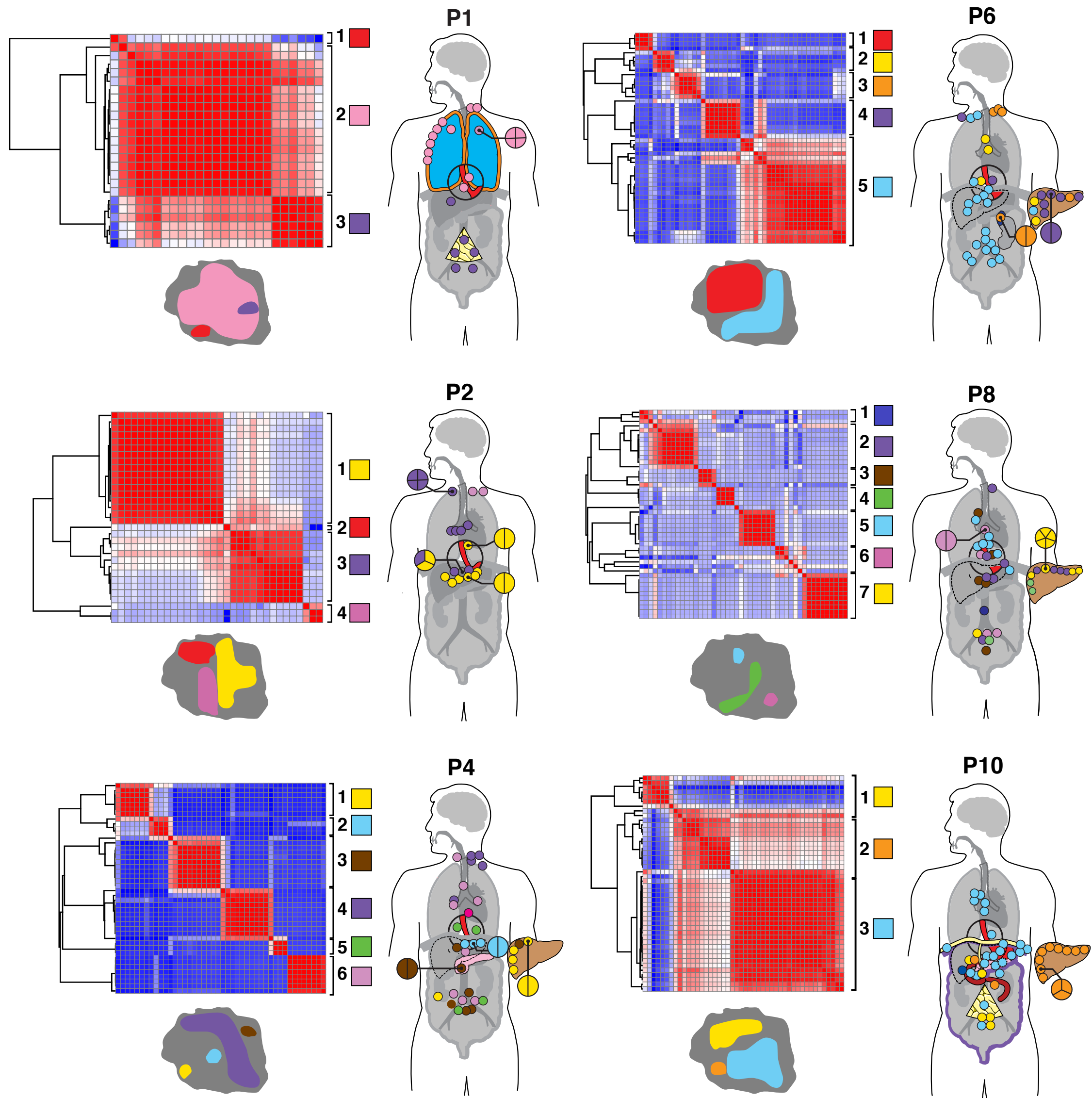
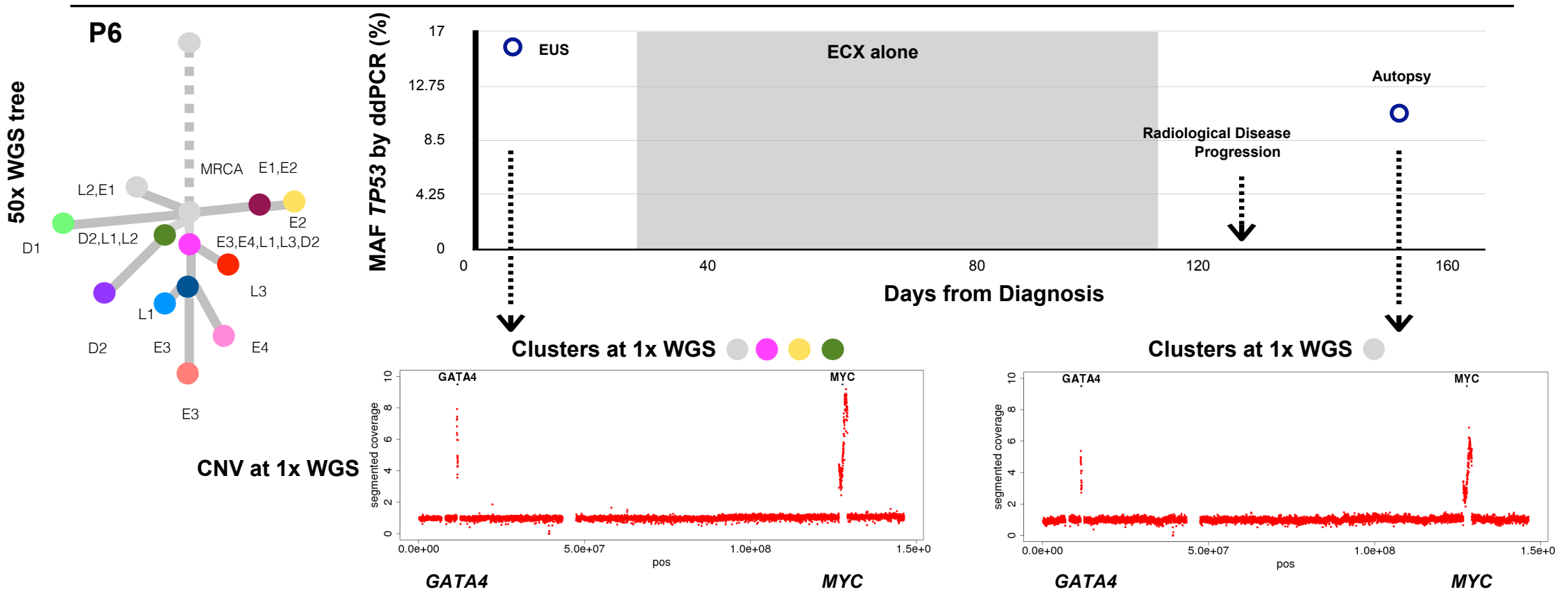
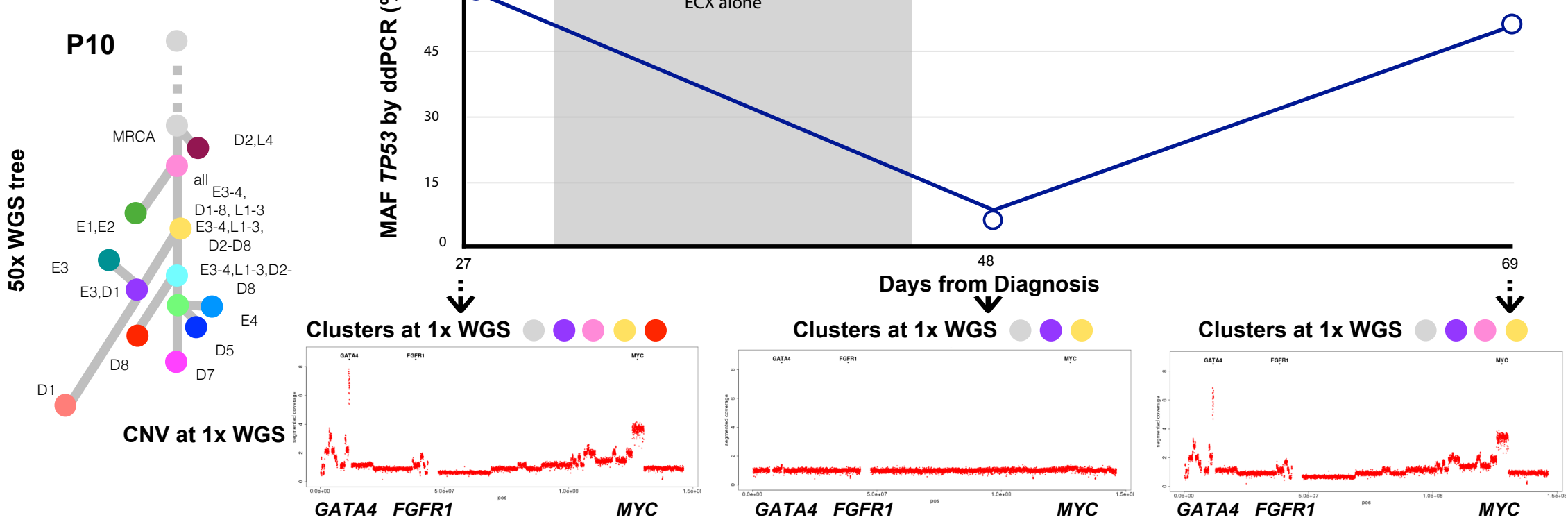


Figure 5 **a**

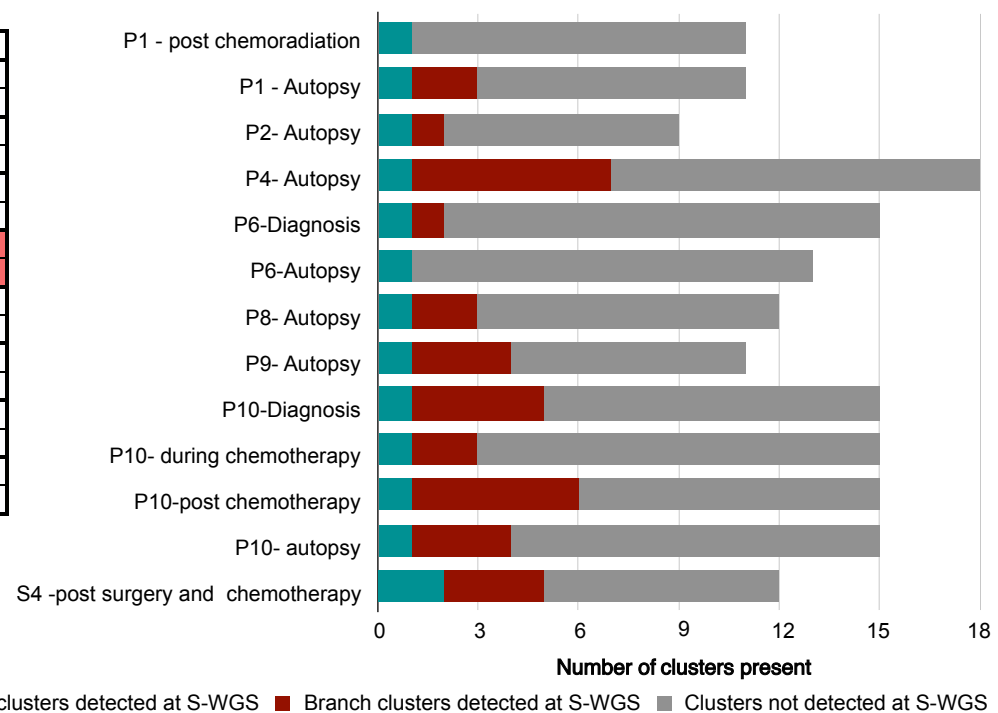


**b**

Case ID		CDK6	CDKN2a	CCND1	CCND3	EGFR	GATA4	KRAS	MYC	MET	PRKC1
P1	Plasma										
	Tissue										
P2	Plasma										
	Tissue										
P3	Plasma										
	Tissue										
P4	Plasma										
	Tissue										
P6	Plasma										
	Tissue										
P8	Plasma										
	Tissue										
P9	Plasma										
	Tissue										
P10	Plasma										
	Tissue										

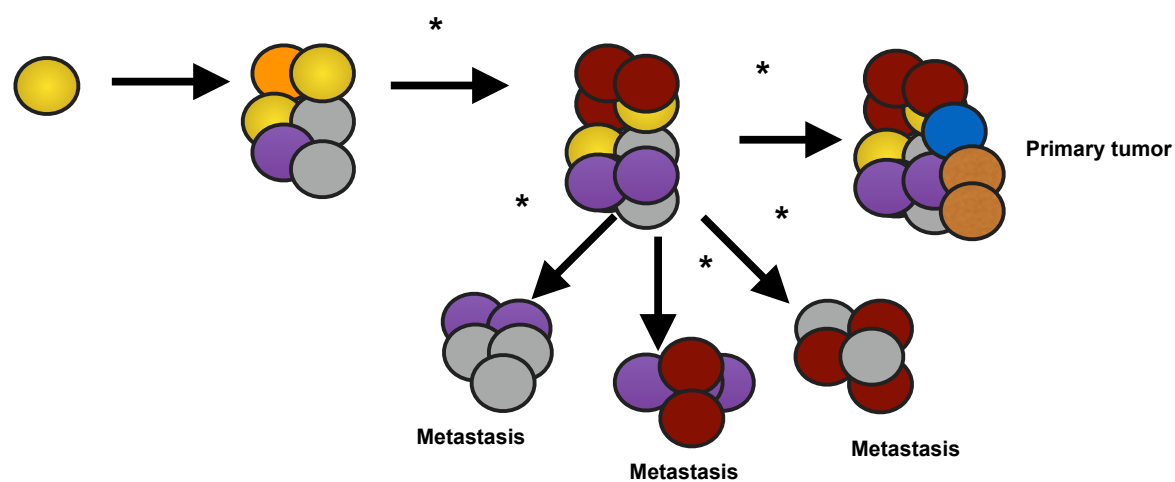
Loss    Unaltered    Amplification

**c**



a

## Diaspora Model of Metastatic Spread



b

## Features of Diaspora

Case	DEFINING	ASSOCIATED			
	Multiple subclones from primary spread to multiple metastatic sites	Stellate pattern of three or more subclones derived from the same ancestor found in metastatic sites	Lack of Signature 1 mutations, indicating rapid accumulation of mutations and near-synchronous spread	Spread of at least one subclone to organs of different types, including both lymph nodes and distant organs	Evidence for selection of subclones within the diaspora, indicative of an evolutionary niche (driver amplifications)
P1	✓	×	✓	*✓	×
P2	✓	✓	✓	✓	✓
P3	✓	×	×	✓	✓
P4	✓	✓	✓	✓	✓
P6	✓	✓	✓	✓	✓
P8	✓	✓	×	*✓	×
P9	✓	✓	×	✓	×
P10	✓	×	✓	✓	×
S3	×	×	×	×	✓
S4	✓	✓	✓	✓	✓